Title:

A kinematic rupture generator for ground-motion simulations: Validation and scenarios in South Iceland

Authors:

Victor M. Hernández-Aguirre[1]

Rajesh Rupakhety[1]

Roberto Paolucci[3]

Manuela Vanini[3]

Chiara Smerzini[3]

Bjarni Bessason[2]

Sigurður Erlingsson[2]

[1] Earthquake Engineering Research Centre, Faculty of Civil and Environmental Engineering, University of Iceland, Austurvegur 2a, 800 Selfoss, Iceland

Email: victorh@hi.is

[2] Faculty of Civil and Environmental Engineering, University of Iceland, Reykjavík, Iceland

[3] Department of Civil and Environmental Engineering, Politecnico di Milano, Milan, Italy

Date of Preprint Posting:

15 May 2026

A kinematic rupture generator for ground-motion simulations: Validation and scenarios in South Iceland

Victor M. Hernández-Aguirre[1] · Rajesh Rupakhety[1] Roberto Paolucci[3] · Chiara Smerzini[3] · Manuela Vanini[3] · Bjarni Bessason[2] · Sigurður Erlingsson[2]

Corresponding author: Victor M. Hernández-Aguirre, victorh@hi.is

[1] Earthquake Engineering Research Center, University of Iceland, Selfoss, Iceland

[2] Faculty of Civil and Environmental Engineering, University of Iceland, Reykjavík, Iceland

[3] Department of Civil and Environmental Engineering, Politecnico di Milano, Milan, Italy

Key points

- We propose a kinematic rupture generator modeling rupture parameters as correlated stochastic spatial fields.
- The rupture generator coupled with the ANN2BB method reproduces records and a local ground-motion model.
- Scenario simulations can supplement records and bound epistemic uncertainty in seismic hazard analyses.

Declaration of Competing Interests
The authors acknowledge there are no conflicts of interest recorded.

Abstract: Physics-based ground-motion simulation can reduce epistemic uncertainty in regions with sparse strong-motion data, but hazard applications require rupture ensembles that are physically plausible, statistically controlled, and computationally efficient. We present a modular kinematic rupture generator for physics-based simulations (PBS) in which final slip, rupture speed ratio (V_R/V_S), and peak slip velocity (V_{max}) are modelled as heterogeneous, mutually correlated spatial fields governed by prescribed one-point statistics and covariance-based two-point structure. The generator supports both event-constrained ruptures (for validation) and fully stochastic scenario ruptures, while enabling systematic propagation of source uncertainty through an effective stress-parameter scaling with V_{max}. We demonstrate the approach using a regional 3D numerical model of South Iceland (accurate up to 1.9 Hz) solved with the spectral-element code SPEED. A broadband extension is obtained via the ANN2BB method. Validation against the June 2000 M_w 6.5 and M_w 6.4 earthquakes shows good agreement between recorded and simulated low-frequency waveforms and response spectra, supported by goodness-of-fit metrics across duration, peak measures, and long-period spectral ordinates. We then generate M_w 6.5 and M_w 7 scenario ensembles and compare their spectral-acceleration attenuation and variability with local and global GMMs. M_w 6.5 scenarios track the Icelandic model within its calibration range, whereas M_w 7 scenarios diverge from extrapolated local predictions, indicating substantial epistemic uncertainty in large-magnitude, short-distance scaling where observations are unavailable. The simulated variability is consistent with empirical expectations, supporting the use of the proposed rupture-generator–PBS framework to produce region-specific, non-ergodic ground-motion ensembles for scenario-based risk analysis and PBS-informed hazard assessment.

INTRODUCTION

A central requirement in seismic hazard and risk assessment is the ability to estimate not only median ground motion (GM) but also the range of plausible outcomes that drive damage and losses. Empirical ground-motion models (GMMs) provide the conventional approach. However, in many regions, sparse strong-motion data from large events limit constraints on region- and path-specific (non-ergodic) effects, as well as near-fault scaling at the magnitudes most relevant to risk, increasing epistemic uncertainty. Furthermore, standard GMMs compress rupture effects into a small set of predictors (e.g., magnitude, distance, fault geometry and mechanism) and therefore cannot explicitly represent how spatiotemporal rupture complexity governs directivity, coherency, and the spatial variability of intensity measures (IMs).

Three-dimensional physics-based simulations (PBS), based on the numerical solution of the elastodynamic equations, provide a complementary framework to (i) develop physics-consistent GM scenarios for risk management (e.g., Detweiler and Wein, 2018; Paolucci et al., 2026), (ii) inform GM modeling (e.g., Moschetti et al., 2024; Sung et al., 2025), and (iii) enable non-ergodic site-specific probabilistic seismic hazard assessment (PSHA) and loss estimation (e.g., Graves et al., 2011; Stupazzini et al., 2021). However, for PBS to be useful in hazard and risk applications, they must be coupled with source descriptions that are both physically plausible and scalable to produce large rupture ensembles. In many practical settings, the dominant modeling uncertainty arises from the earthquake source: rupture complexity controls near-fault directivity (Mavroeidis and Papageorgiou, 2010) and the spatial variability of IMs (e.g., Crempien and Archuleta, 2017; Akinci et al., 2024), thereby strongly influencing hazard and risk estimates. Hazard-oriented applications therefore require rupture models that can be generated repeatedly, with controlled variability and physically motivated parameter dependence, and that reproduce not only median shaking but also the IM variability that controls tail risk.

In PBS, earthquake sources are represented either kinematically or dynamically. Kinematic models prescribe slip evolution through fields such as final slip, rupture time, rise time, and rupture speed, offering computational efficiency and flexibility but lacking explicit stress–friction physics. Dynamic rupture models, by contrast, provide self-consistent rupture evolution by coupling elastodynamics to frictional constitutive laws (Harris, 2004), but their computational cost and parameter complexity often preclude the simulation of a large number of scenarios required for hazard applications. Pseudo-dynamic approaches (Guatteri et al., 2004) bridge these extremes by constructing kinematic descriptions that emulate salient features of dynamic ruptures while remaining efficient for repeated simulations. Some existing pseudo-dynamic rupture generators leverage statistical relationships among kinematic parameters inferred a posteriori from dynamic rupture simulations (Schmedes et al., 2013; Song, 2016; e.g., Savran and Olsen, 2020), and recent machine-learning formulations have been proposed to capture nonlinear dependencies and incorporate fault-roughness effects (Aquib et al., 2025). Despite this progress, a persistent practical need in PBS-based hazard studies is a modular rupture generator that (i) is suitable to produce rupture ensembles efficiently, (ii) enforces inter-parameter dependence (rather than ad hoc independent sampling), (iii) supports systematic propagation of epistemic uncertainty in rupture intensity, and (iv) is readily adjustable as new constraints on source parameters become available.

Widely used kinematic rupture generators for scenario simulation—most notably the Graves and Pitarka family (Graves and Pitarka, 2010, 2015; Pitarka et al., 2022)—have been developed and refined primarily through validation exercises targeting earthquakes in the United States. While such approaches are powerful within their calibration domain, direct transfer to data-scarce regions with distinct crustal structure and source characteristics is not straightforward. In addition, for hazard-oriented scenario ensembles they do not provide an explicit, region-portable statistical mechanism to propagate epistemic uncertainty in rupture intensity through controlled variability in rise time (τ_R) /peak slip velocity (V_{max}) and its scaling with stress drop, which is central when assessing how source uncertainty maps into IM variability.

This study introduces a modular kinematic rupture generator that addresses these needs within a covariance-based pseudo-dynamic framework. Building on key elements from Song et al. (2016) (SO16), Savran and Olsen (2020) (SO20), and Aquib et al. (2025) (AM25), the generator represents slip, rupture speed ratio, that is earthquake crack propagation velocity relative to the shear wave velocity, (V_R/V_S), and V_{max} as heterogeneous and mutually correlated spatial random fields governed by prescribed one-point statistics and covariance-based two-point structure. Relative to SO20, we introduce two practical extensions: (i) the slip field is generated using a flexible stochastic model separately from the joint prior, which increases modeling freedom (e.g., alternative slip correlation structures) and enables representation of historical earthquakes via prescribed deterministic/hybrid slip models; and (ii) V_{max} is scaled through magnitude-conditioned stress-drop sampling, allowing epistemic uncertainty in rupture intensity to be propagated systematically into simulated ground motions. The framework is tunable in complexity and variability and is intended to support systematic quantification of how source uncertainty maps into IM variability in PBS-based scenario ensembles.

We demonstrate the proposed rupture generator using South Iceland as a relevant testbed. The target region includes an active transform system capable of producing damaging strike-slip earthquakes, with limited strong-motion observations at larger magnitudes. This combination—moderate-to-high hazard relevance and sparse near-field data—provides a stringent setting in which the ability to generate credible rupture ensembles is particularly important.

The objectives of this work are therefore: (1) to develop a kinematic rupture generation framework suitable for generation of large ensembles; (2) to construct and validate a 3D simulation model for South Iceland; and (3) to perform scenario simulations to assess both median shaking levels and variability arising from the rupture generator, as a step toward using PBS products in PSHA and in non-ergodic GM modeling. The remainder of the paper is organized as follows. We first present the rupture generation framework, the 3D model setup and the method to extend the PBS results to higher frequencies. We then validate simulations of the June 2000 South Iceland earthquakes (M_w 6.4 and 6.5) using recorded data and goodness-of-fit (GoF) metrics and analyze near-fault characteristics. PBS are performed with the open-source spectral-element code SPEED (Mazzieri et al., 2013). Finally, we use the validated framework to simulate scenario events (M_w 6.5 and M_w 7) and evaluate the resulting spectral accelerations relative to global and local GMMs, with particular emphasis on how rupture-generated variability manifests in IMs.

KINEMATIC RUPTURE GENERATION

In kinematic source modeling, the finite fault is discretized into sub faults, each parameterized by (i) the coseismic slip distribution, (ii) a local source time function (STF), and (iii) the rupture time controlling slip onset at that location. Common STF parameterizations are controlled by a rise time, τ_R, which sets the local slip duration, and in some formulations also by a time-to-peak parameter (acceleration time), T_{acc}, that specifies when the peak slip velocity V_{max} occurs (Tinti, 2005). The rupture time field, $T_R(\mathbf{x})$, is governed by the hypocenter location and the rupture speed $V_R(\mathbf{x})$. The source description is completed by specifying the unit normal vector $\mathbf{n}$ and slip direction $\mathbf{v}$, consistent with the fault geometry (including possible non-planarity) and the (possibly heterogeneous) rake distribution.

Kinematic rupture parameters are not independent: coseismic slip, rise time, rupture speed, and peak slip velocity are coupled through the evolving stress state and frictional resistance along the fault. Empirical and simulation-based studies indicate that rise time tends to increase with slip (Oglesby and Day, 2002; Guatteri et al., 2003; Schmedes et al., 2010; Song et al., 2014; Mai et al., 2017), rupture speed correlates positively with peak slip velocity (Bizzarri, 2012; Mai et al., 2017; Song et al., 2014), and rupture speed may exhibit a weak correlation with slip (Oglesby and Day, 2002; Guatteri et al., 2003). Importantly, allowing spatial variability in τ_R and/or V_{max}, as well as V_R, provides a practical mechanism to represent small-scale rupture heterogeneity, which is known to strongly influence the excitation of mid- to high-frequency GM components (Madariaga, 1977; Spudich and Frazer, 1984; Guatteri et al., 2003; Imperatori and Mai, 2012).

In this section, we describe the steps of the proposed rupture-generation procedure, which is summarized in Figure 1. The framework is organized as a sequence of steps in which a heterogeneous slip distribution is generated first, after which the remaining rupture-parameter fields are obtained using a spatial covariance and cross-field correlation model together with prescribed marginal distributions. We also incorporate fault-roughness effects to represent additional small-scale complexity. This structure preserves physically motivated inter-parameter dependence while enabling efficient generation of rupture ensembles for PBS.

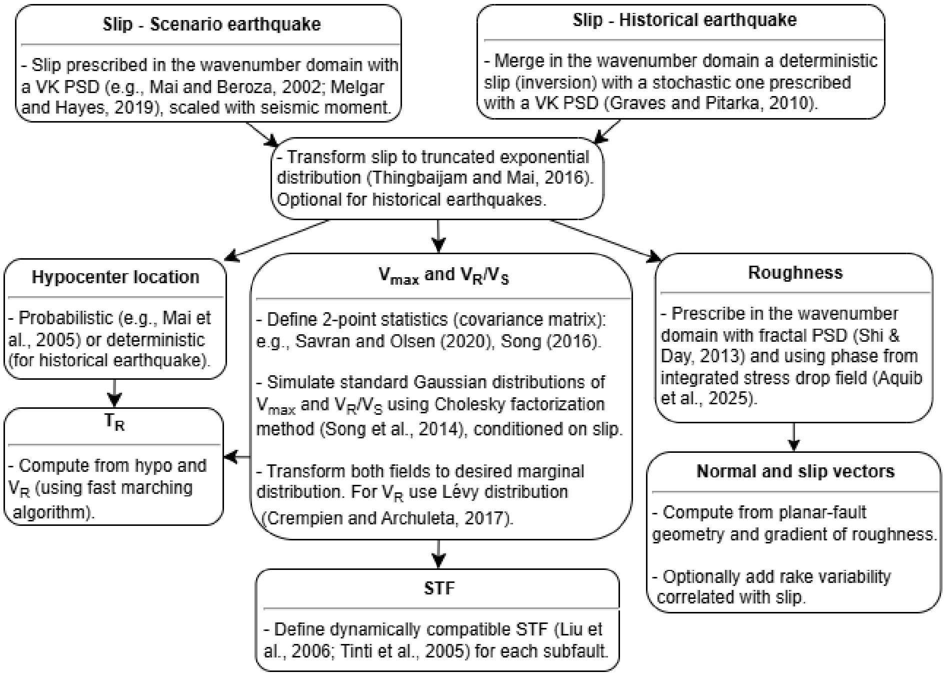

Figure 1. Workflow of the adopted kinematic rupture generation framework.

Slip distribution

The first step of the rupture generator is the synthesis of a heterogeneous slip field over the discretized fault plane. For scenario earthquakes, fault dimensions can be defined from existing scaling laws (e.g., Thingbaijam et al., 2017), or from inversion studies for historical earthquakes. We prescribe the slip distribution $\mathrm{U}(\mathbf{x})$ as a spatially random field following Mai and Beroza (2002), using a von Kármán (VK) power spectral density (PSD) in the wavenumber domain

$$\mathrm{U_{PSD}}\,(\mathrm{k_s}, \mathrm{k_d}) = \frac{1}{[1+(\mathrm{k_s C_s})^2+(\mathrm{k_d C_d})^2]^{\mathrm{H}+1}} \tag{1}$$

where k_s and k_d are the wavenumbers along the strike and dip, respectively, H is the Hurst exponent, and C_s and C_d are the correlation lengths along the strike and dip, respectively, which scale with fault dimensions. Melgar and Hayes (2019) and Mai and Beroza (2002) propose values for the parameters of the slip VK PSD. The spectral synthesis method (Ogorodnikov and Prigarin, 1996) is used to generate synthetic U fields in the wavenumber domain with the prescribed VK PSD. This method results in a Gaussian random field that should be scaled to the target seismic moment M_0.

Following AM25, the normally distributed scaled slip values are transformed to follow a truncated exponential distribution (Thingbaijam and Mai, 2016), parametrized by the mean slip (U_{μ}), and maximum slip, (U_{max}). This is achieved by using a rank transform, i.e., by replacing the k^{th} value of simulated distribution with the k^{th} value sampled from the target distribution. Finally, the slip is tapered at the lateral and bottom boundary and re-scaled to maintain the desired seismic moment.

The resulting slip distributions may result in asperities located in any part of the fault. Since it is known that most of the slip tends to be concentrated in the central part of the fault (e.g., Manighetti et al., 2005), we added a condition to accept a distribution, i.e., that at least 60% of the total slip must lie within the central portion of the fault plane, defined as the area bounded by the central 50% of the fault length and the central 50% of the fault width.

For simulating historical earthquakes we follow the approach of Graves and Pitarka (2010) to merge a deterministic slip distribution, usually coming from inversions, with a stochastic portion prescribed as just described. However, as scaling factor (s) for the stochastic portion $\hat{Z}(k)$ we use

$$s = \frac{\sum_{|\mathbf{k}|\le k_c} |\hat{D}(k)|}{\sum_{|\mathbf{k}|\le k_c} |\hat{Z}(k)|} \tag{2}$$

where **k** is the wavenumber, and k_c is the corner wavenumber of the merging filter. This ensures that the spectra of the stochastic and deterministic portions $\hat{D}(k)$ are closer to each other in the range $|\mathbf{k}| \le k_c$, and not only at **k**=0, as the original method implies.

Hypocenter location

Because rupture directivity is strongly influenced by hypocenter location relative to a site (Somerville et al., 1997; Spudich and Chiou, 2008), scenario simulations require a defensible prescription of the hypocenter on the fault plane; however, its location is uncertain for future events. Importantly, hypocenters are not expected to be uniformly random distributed over the fault plane; instead, their occurrence can be statistically related to the slip distribution and the location of high-slip asperities (Somerville et al., 1999; Mai et al., 2005; Manighetti et al., 2005; Melgar & Hayes, 2019). Accordingly, given the previously generated slip field, we construct a two-dimensional probability density function (PDF) for hypocenter location $p\big(x_h \mid U(x)\big)$ using the statistical model of Mai et al. (2005), which accounts for faulting style, slip at the hypocenter, and distance to high-slip asperities. The hypocenter location is then randomly sampled from this conditioned PDF. The same approach is adopted by AM25. The hypocenter location for historical events can be set deterministically based on available information.

Fault roughness

Natural faults are well known to deviate from planarity and have micro- to macro-scale complexities (10^{-9} - 10^{3} m) that can be described as self-similar fractals (Power and Tullis, 1991; Candela et al., 2012). This nonplanarity is referred to as roughness, that is, out-of-plane topographic variations of the fault surface. Inclusion of fault roughness improves PBS, by enhancing high-frequency radiation through rupture-front acceleration/deceleration and reduces high-frequency coherency—moving simulations toward observed statistics (e.g., Dunham et al., 2011; Shi and Day, 2013; Graves and Pitarka, 2016).

We include fault roughness, based on the physically consistent method of AM25, in which a stress drop (ISD) field is constructed by integrating stress drops along strike and dip. A zero-mean random-phase fractal field is then generated (Shi and Day, 2013), with amplitudes scaled to the target roughness parameter α, which is usually in the range of 10-3 to 10-2 (Power and Tullis, 1991). Finally, the phase of the ISD field is merged with the amplitude of the fractal field in the wavenumber domain, and the roughness field is obtained via inverse Fourier transform.

Normal and slip vectors

The unit normal vector **n** and slip-direction vector **v** are defined by the fault geometry and the rake angle λ. Finite-fault inversions commonly allow for, and often recover, spatially variable rake over the rupture plane (e.g., Liu and Archuleta, 2004), reflecting the influence of fault geometry, local stress heterogeneity, and rupture dynamics. Motivated by this, we model the rake distribution $\lambda(\mathbf{x})$ as a two-dimensional random field on the fault plane, using the same spatial correlation model as the slip field $\mathrm{U}(\mathbf{x})$, together with a prescribed mean value consistent with the source mechanism and a standard deviation of 10°. This treatment is similar to the approach of Graves and Pitarka (2010), who introduce a spatially variable rake, although with a wider variability range of about ±15°.

Having computed $\lambda(\boldsymbol{x})$ and the non-planar fault-geometry in previous section, $\mathbf{n}(\mathbf{x})$ and $\mathbf{v}(\mathbf{x})$ at each sub fault are computed from the gradient of the perturbed fault surface as described in Graves and Pitarka (2016). Each point source is then placed at its off-planar location.

$\mathbf{V_{max}}$ and $\mathbf{V_R}$

A number of studies have proposed statistical frameworks for earthquake source process, modeling it as a multivariate Gaussian process, parameterized through 1-point and 2-point statistics of source properties (Schmedes et al., 2013; Song et al., 2014; Savran and Olsen, 2020). The 1-point statistics describe the marginal PDF of each rupture parameter. In contrast, the 2-point statistics provide information on spatial dependencies: they capture both the autocorrelation structure within a single parameter's spatial distribution and the cross-correlations between different rupture parameters. Collectively, these statistics define the covariance matrix of the multivariate Gaussian distribution, which governs the joint variability of the source model. Importantly, both 1-point and 2-point statistics are typically derived from ensembles of dynamic rupture simulations, ensuring that the statistical representation reflects physically consistent rupture behavior.

SO16 and SO20 model the fields U, $\mathrm{V_{max}}$, and $\mathrm{V_R/V_S}$ as a multivariate Gaussian distribution with zero mean and covariance matrix $\mathbf{\Sigma}$. They propose covariance models based on the analysis of simulations from earthquakes in the magnitude range from 6.5 to 7 and 7.2, respectively. Given $\mathbf{\Sigma}$, random fields of these parameters can be jointly simulated.

We adopt the covariance model proposed by SO20, which consists of the following linear model of coregionalization (LMC) that assumes second-order stationarity and isotropy (dependence only on separation distance h)

$$\mathbf{\Sigma}(\mathrm{h}) = \mathbf{B}^1 \exp\left(-\frac{3\mathrm{h}}{\mathrm{a_{ss}}}\right) + \mathbf{B}^2 \exp\left(-\frac{3\mathrm{h}}{\mathrm{a_{ls}}}\right), \tag{3}$$

where $\mathrm{a_{ss}}$ and $\mathrm{a_{ls}}$ represent the short-scale and long-scale range parameters, respectively, and matrices $\mathbf{B^1}$ and $\mathbf{B^2}$ are the short-scale and long-scale coregionalization matrices, respectively. Given that $\mathbf{B^1}$ and $\mathbf{B^2}$ are positive semidefinite, this model guarantees positive definiteness, and so the Cholesky factorization simulation method can be used. Since in our implementation the slip distribution is prescribed independently, we simulate the fields $\mathrm{V_{max}}$ and $\mathrm{V_R/V_S}$ from their distribution conditional on U, as explained in the Electronic Supplement.

Marginal distributions

The outputs from the previous step are two zero-mean Gaussian random fields $\mathrm{V_{max}}$ and $\mathrm{V_R/V_S}$, that are then transformed to any desired distribution. We use a Gaussian-copula (rank) transform; this preserves the dependence structure in a rank sense while enforcing the desired marginals. As previously mentioned, $\mathrm{V_R}$ highly influences the generation of mid-to high-frequencies, but also directivity effects (Spudich and Frazer, 1984). Therefore, accurate representation of its marginal distribution is critical for broadband GM simulation. SO16 assumes a Gaussian distribution for $\mathrm{V_{max}}$ and $\mathrm{V_R/V_S}$ fields and provides values for the mean and standard deviation, while on the other hand, Schmedes et al. (2013) and Savran and Olsen (2020) use arbitrary empirical distributions from the analyzed dynamic simulations. The mean of the ratio $\mathrm{V_R/V_S}$ is rather well constrained, and usually assumed to be in the range 0.7 to 0.85 (Geller, 1976; Graves and Pitarka, 2010). We adopt a Lévy distribution for $\mathrm{V_R/V_S}$ as proposed by Crempien and Archuleta (2017) for the UCSB rupture generator, with parameters of first shape α=1.4, of second shape

β=-0.95, scale γ=0.04, and location (mode) δ=0.82. Moreover, we limit V_R/V_S to the interval [0.2, 0.95]. With these parameters the mean $\bar{V}_R$ is ~0.78 V_S.

We highlight that U and V_{max} (or τ_R) are the parameters controlling the low and high-frequency ends of the radiated spectra, respectively (Beresnev, 2022). Therefore, V_{max} has a strong influence on the simulated GM. From laboratory experiments (Ohnaka and Yamashita, 1989) and results of dynamic simulations (Tinti, 2005) it has been proposed that V_{max} scales as

$$V_{max} \propto C(V_R)\Delta\sigma_b \quad (4)$$

where $C(V_R)$ is a function of V_R and $\Delta\sigma_b$ is the breakdown stress drop. Under a slip-weakening law with no overshoot (Ida, 1972), $\Delta\sigma_b = \Delta\sigma_s + SE$, where $\Delta\sigma_s$ is the static stress drop and SE is the strength excess. Assuming that the ratio $\alpha \equiv SE/\Delta\sigma_s$ is approximately constant within a region and magnitude-independent, implies that $\Delta\sigma_b = (1+\alpha)\Delta\sigma_s$, so Eq. (4) can be rewritten as $V_{max} \propto C(V_R)\Delta\sigma_s$. Assuming sub-shear ruptures such that $\bar{V}_R$ (and hence $C(V_R)$) is relatively constant, we calibrate the resulting linear relation using the mean $\bar{V}_{max} = 1.5$ m/s proposed by SO20 at the mean stress drop of their dynamic simulations $\overline{\Delta\sigma_s} = 5$ MPa, obtaining

$$\bar{V}_{max}\,[\mathrm{m/s}] = 0.3 \cdot \overline{\Delta\sigma}\,[\mathrm{MPa}]. \quad (5)$$

Hereafter we use $\overline{\Delta\sigma}$ as an effective stress drop, i.e., a stress parameter in the sense of stochastic simulation that represents rupture strength and controls the high-frequency spectral level, rather than a uniquely defined static stress drop inferred from final slip and source dimensions (Boore, 1983; Cotton et al., 2013). Some studies based on the analysis of rupture models report that $\Delta\sigma$ increases with magnitude (e.g., Causse et al., 2014; Thingbaijam et al., 2017). Consistently, Bizzarri (2012) observed the scaling $V_{max} \propto M_0^{0.18}$ from dynamic simulations. Therefore, to incorporate possible magnitude dependence of stress drop, we model the $\overline{\Delta\sigma}$ (MPa) conditional on M_w as a truncated lognormal distribution following Causse et al. (2014)

$$\log_{10}(\overline{\Delta\sigma}) = a \cdot M_w + c + \tau_{\Delta\sigma}\,\varepsilon, \qquad \varepsilon \sim \mathcal{N}(0,1) \text{ truncated to } |\varepsilon| \leq 2. \quad (6)$$

Causse et al. (2014) propose a=0.27, c= -1.071 (converted from their original expression in terms of M_0), and $\tau_{\Delta\sigma} = 0.3$. A lognormal model for $\overline{\Delta\sigma}$ has been also proposed by other authors (Baltay et al., 2011; Cotton et al., 2013). To slightly reduce the magnitude-dependence, which not all studies support (e.g., Abercrombie, 2021), we use a=0.2. We computed c= -0.641 to get $\overline{\Delta\sigma}$ = 5 MPa at M_w= 6.7, matching the average reported for the SO20 dynamic-simulation dataset. Regional departures from the global $\overline{\Delta\sigma}$ can be represented by shifting c accordingly. Alternatively, when regional stress drop estimates (and associated variability) are available, $\overline{\Delta\sigma}$ can be prescribed directly and Eq. (6) is bypassed.

We model $V_{max}(\mathbf{x})$ as a normal random field with mean given by Eq. (5) and standard deviation $\sigma_{V_{max}}$= 1 m/s. We then truncate $V_{max}(\mathbf{x})$ to the interval [0.05, 10] m/s. The upper limit of 10 m/s is motivated by dynamic simulations on rough faults indicating large localized slip velocities (Bizzarri, 2012; Mai et al., 2017; Savran and Olsen, 2020). In this hierarchical formulation $\bar{V}_{max}$ is a stochastic (latent) variable derived from $\overline{\Delta\sigma}$ through Eq. (5).

Finally, due to the intrinsic coupling between τ_R and V_{max}, low V_{max} values in regions of substantial slip can yield unrealistically large τ_R. To avoid this issue, the U/V_{max} ratio is constrained to a maximum value of 4, consistent with SO20.

Source time function

Among the most widely adopted choices for STF are the regularized Yoffe function (Tinti, 2005) and the Liu et al. (2006) approximation of the STF proposed by Guatteri et al. (2004), both of which align closely with results from dynamic rupture simulations. These functions have three parameters U, τ_R, and T_{acc}. In the present framework, however, V_{max} is specified directly, rather than τ_R, requiring τ_R to be determined a posteriori. Originally Liu et al. (2006) used $\mathrm{T}_{\mathrm{acc}} = 0.13\tau_{\mathrm{R}}$, however we use Liu's STF with $\mathrm{T}_{\mathrm{acc}}$ as a free parameter.

Finally, because $\mathrm{T}_{\mathrm{acc}}$ and $\mathrm{V}_{\mathrm{max}}$ are expected to be negatively correlated (e.g., Mai et al., 2017; Schmedes et al., 2010), we model $\mathrm{T}_{\mathrm{acc}}(\mathbf{x})$ as a spatial random field that is anticorrelated with $\mathrm{V}_{\mathrm{max}}(\mathbf{x})$. The field is generated using the same spatial correlation structure as $\mathrm{V}_{\mathrm{max}}$ (i.e., $\mathbf{\Sigma}_{33}$), with a target correlation coefficient of -0.4, and is then rescaled to match a prescribed mean and standard deviation. These target moments may be selected from the literature (e.g., Schmedes et al., 2013), or calibrated for the region of interest, considering that a lower $\mathrm{T}_{\mathrm{acc}}$ enhances the generation of higher frequencies.

GROUND-MOTION SIMULATIONS FOR SOUTH ICELAND

In this section we describe the numerical model for South Iceland, the specific parameters of the rupture models, and the hybrid broadband generation method.

Tectonic framework

Iceland is the most earthquake-prone country in northern Europe. Most of its seismic activity is linked to the mid-Atlantic plate boundary that runs through the country. One of the most seismically active segments of this plate boundary is the South Iceland Seismic Zone (SISZ), which is an approximately 80-km-long transform zone (see Figure 2) accommodating left-lateral shear along its East-to-West trend. The SISZ is characterized by arrays of N–S right lateral strike-slip faults, spaced 2–5 km apart (Clifton and Einarsson, 2005). Four damaging earthquakes have occurred in the SISZ since 1900 (Jónasson et al., 2021): a M_S 7 on 6 May 1912 in its eastern part, a M_w 6.3 on 29 May 2008 in its westernmost part, and a M_w 6.5 and M_w 6.4 during the June 2000 sequence (see Figure 2). The potential of the SISZ of producing destructive earthquakes as large as M_w 7, combined with the fact that it is one of the most densely populated areas where important infrastructure is located, makes it the region where seismic hazard and risk is the highest in Iceland (Sigbjörnsson and Rupakhety, 2014; Rupakhety et al., 2016; Kowsari et al., 2023).

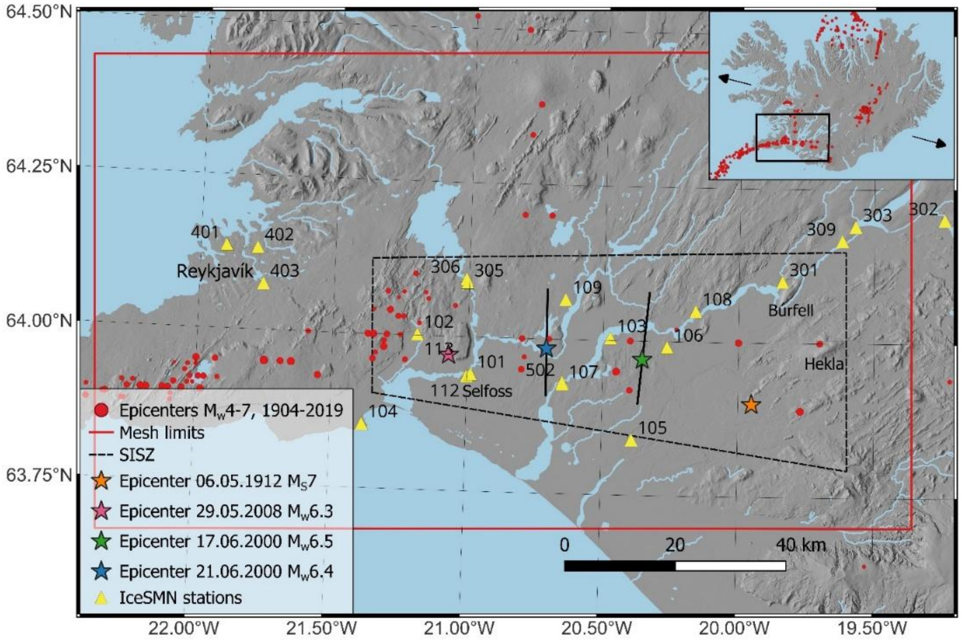

Figure 2. Map of South Iceland. Stars indicate the epicenters of the M_w 6.5 17 June 2000 and M_w 6.4 21 June 2000 earthquakes, while black lines are their fault traces. Red circles are the epicenters of significant earthquakes from 1904 to 2019 (Jónasson et al., 2021).

The June 2000 South Iceland sequence began on 17 June 2000 with a mainshock of magnitude M_w 6.5. Three and a half days later, an earthquake of magnitude M_w 6.4 ruptured around 17 km to the west of the mainshock. These events are used for validation in the next section and were recorded by the stations of the Icelandic Strong-Motion Network (IceSMN, Rupakhety & Ólafsson, 2015), shown in Figure 2.

Seismic velocity model and anelastic attenuation model

The surface geology of the South Iceland Lowland reflects volcanic activity, glacial deposition, and sea-level changes. Sedimentary deposits are commonly overlain or interbedded with thin post-glacial basaltic lava and hyaloclastite, producing layered near-surface conditions (Olafsdottir et al., 2023). This heterogeneous shallow structure, further complicated by fractures and faults, can amplify high-frequency GM (e.g., Darzi et al., 2024). Accurately modeling these site-effects with deterministic PBS would require both a very fine computational mesh and detailed site characterization, which is not available. Therefore, we restrict our numerical model to bedrock conditions.

The adopted shear-wave velocity model in the simulations consists of a parabolic profile fitted to the horizontally-layered upper crustal model proposed by from Dubois et al. (2008), with the difference that we reduced the V_S at the ground surface from 2150 m/s to 1400 m/s. For the density (ρ) we also considered a parabolic variation with depth. Compressional-wave velocity (V_P) is defined as $1.8 \cdot V_S$. V_S (in m/s) and ρ (in kg/m^3) are computed as follows:

$$\begin{aligned} V_S = 1400 + 37 \cdot z^{0.48},\ \ \rho = 2200 + 4.6\ \cdot z^{0.58}, &\quad \text{for } z < 5000 \text{ m}, \\ V_S = 3900,\ \ \rho = 2950, &\quad \text{for } z \geq 5000 \text{ m}, \end{aligned} \tag{7}$$

where z is the depth from the topographic surface. The variation of V_S with depth is shown in Figure S1a of the Electronic Supplement.

We use a visco-elastic constitutive model with a frequency-dependent quality factor ($Q = Q_0 \cdot f/f_0$), with $Qs_0 = 0.03 \cdot V_S$ and $Qp_0 = 1.5Qs_0$, and reference frequency $f_0 = 1$ Hz. The low Qs_0 reflects the high attenuation in the upper crust caused by strong near-surface seismic heterogeneity in Iceland (Menke et al., 1995).

Numerical model

The numerical model for South Iceland includes both the topography inland and the bathymetry offshore. The computational mesh spans approximately 138x90x25 km^3 (Figure S1b) and was generated using the meshing software Cubit (Coreform-LLC, 2025) through a Python wrapper (CubitPython4SPEED). The mesh is designed to achieve accurate wave propagation up to fmax = 1.9 Hz, to limit the computational cost. Simulations were performed on the Elja cluster at the University of Iceland using the open-source spectral-element code SPEED (Mazzieri et al., 2013), which employs hexahedral elements with high-order Lagrange interpolation. We use a polynomial degree SD =3 and target approximately 5 spectral nodes per minimum wavelength throughout the domain; for SD=3 and f_{max} = 1.9 Hz, that implies a minimum surface element size of ~330m and minimum nodal grid spacing of ~100 m. Overall, the mesh consists of 1.67×10^6 spectral elements, resulting in approximately 46.3×10^6 degrees of freedom.

Kinematic rupture models

To simulate the 2000 South Iceland events, the slip distributions are defined by merging a stochastic portion with the slip distributions obtained via a joint inversion by Dubois et al. (2008), as previously described. The other global source parameters, i.e., hypocenter location, fault location and geometry, are also taken from Dubois et al. (2008). After some initial tests we decided to use a mean $\overline{T}_{acc} = 0.2\tau_R$, with the aim of enhancing the generation of long-period motion, which has been observed to be larger in South Iceland with respect to other tectonic regions. Moreover, since it is known that stress-drop of tectonic earthquakes in Iceland is larger than the global average (Bjarnason and Einarsson, 1991; Hensch et al., 2016), we adopt $\bar{V}_{max}$= 2.5 m/s for these simulations, which implies $\Delta\sigma$ = 8.33 MPa from Eq. (5)

and a regional constant c = -0.379 from Eq. (6). The rest of source parameters, shown in Figure 3 for the 21 June 2000 earthquake and in Figure S2 for the 17 June 2000 earthquake, are prescribed as described in the previous section.

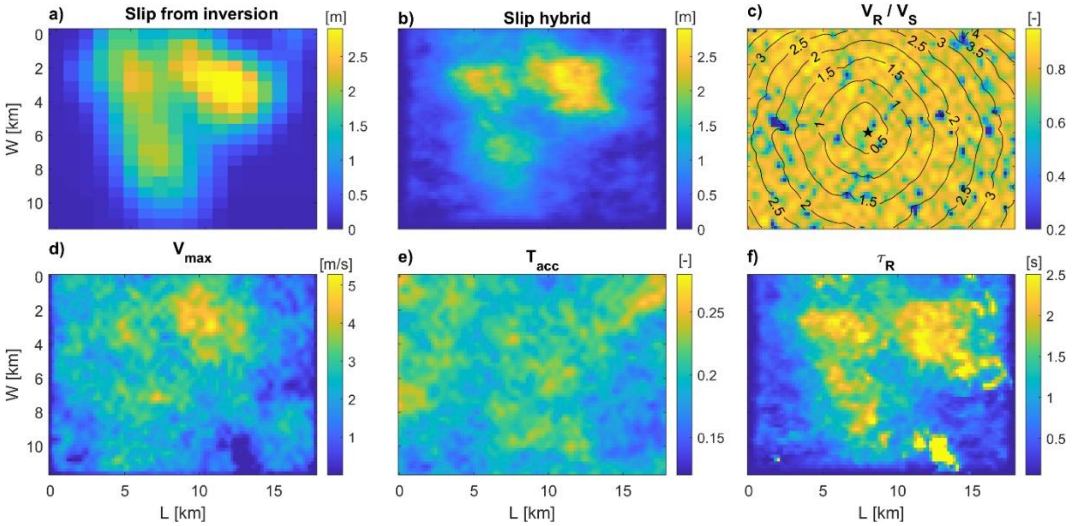

Figure 3. Kinematic source parameters for the 21 June 2000 M_w 6.4 earthquake. (a) Deterministic slip obtained from Dubois et al. (2008). (b) Hybrid slip distribution. The distributions of V_R/V_S (c) and V_{max} (d) are generated from a joint distribution conditioned on the slip. T_{acc} (e) is a prescribed as a correlated random field with V_{max}. τ_R (f) is the rise time. The contour lines in panel (c) represent T_R, while the star is the hypocenter location.

Rupture models of recent large events in South Iceland (Dubois et al., 2008; Decriem et al., 2010) indicate smaller fault dimensions than predicted by common scaling laws for shallow crustal strike-slip earthquakes (e.g., Thingbaijam et al., 2017). This is expected since rupture area (S), scales as $S \propto (M_0/\Delta\sigma_s)^{2/3}$ (Aki, 1972), and $\Delta\sigma_s$ in Iceland is above the global average. Therefore, for scenario earthquakes we prescribe fault dimensions from the effective source-area scaling law of shallow crustal strike-slip earthquakes of Mai and Beroza (2000), which has been previously used for Iceland (Bayat et al., 2022) and leads to areas consistent with observed dimensions of historical events.

A total of 30 M_w 6.5 and 20 M_w 7 scenarios were simulated. Values of $\overline{\Delta\sigma}$ were sampled from Eq. (6) with the calibrated regional constant c = -0.379. We adopted $\tau_{\Delta\sigma}$= 0.15. Roughness is included considering α=0.005. For each scenario, 1700 synthetic records were generated. In Figure 4 and Figure S3 we show the rupture models for two M_w 6.5 and two M_w 7 scenarios, respectively. Moreover, Figure 5 shows the total seismic moment rate release as a function of time and its Fourier amplitude spectrum (FAS) for the two M_w 6.5 scenarios. The FAS of the moment rate follows the expected f^{-2} high-frequency decay (Brune, 1970).

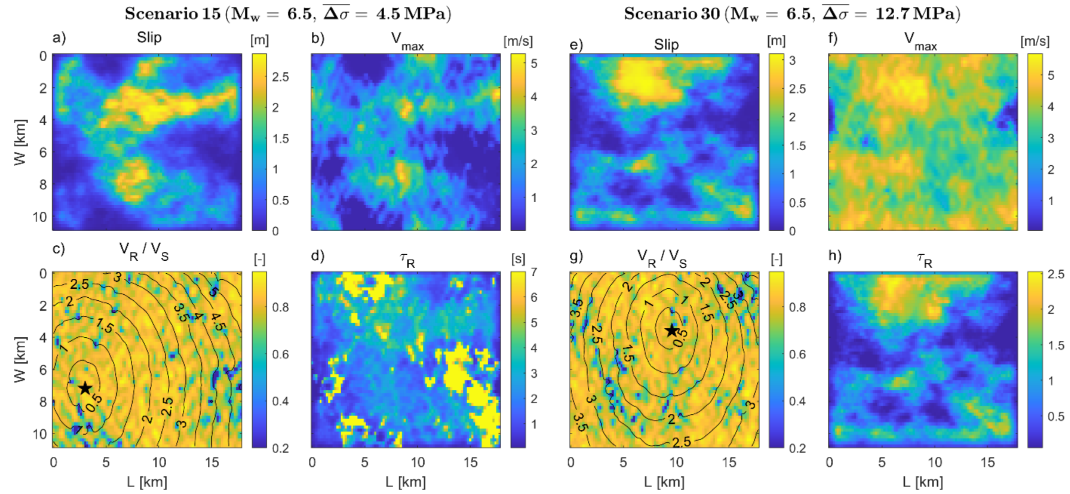

Figure 4. Kinematic source parameters for M_w 6.5 earthquake scenarios 15 (panels a to d) and 30 (panels e to h).

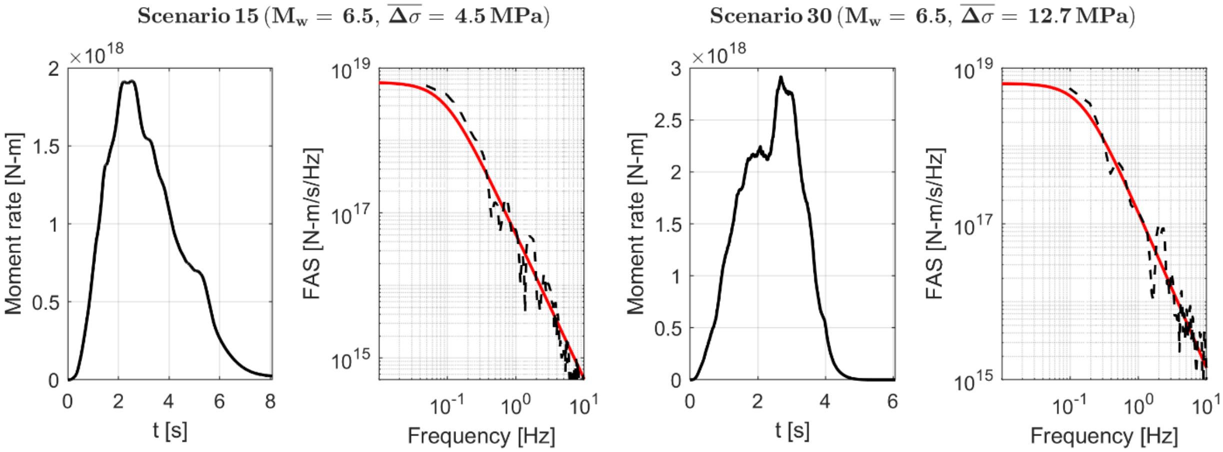

Figure 5. Time evolution of total moment rate and its corresponding Fourier amplitude spectrum (FAS) for scenario 30 (left) and scenario 15 (right) shown in Figure 4. The solid lines are reference source spectra that decay as f^{-2} at large frequencies (Brune, 1970).

Broadband generation - ANN2BB method

For PBS results to be applicable in engineering applications, their energy content must be extended to higher frequencies. We generate broadband (BB) motions using the ANN2BB method originally proposed by Paolucci et al. (2018) and enhanced by Hernández-Aguirre et al. (2026), which uses artificial neural networks (ANNs) to produce three-component BB signals with PBS-consistent long-period content. The procedure consists of three main steps:

(1) Prediction of high-frequency (HF) response spectra, $SA(T < T^*)$, for the three components (two horizontals and vertical). We first compute the median $SA(T < T^*)$ using an ANN that takes as inputs the low-frequency (LF) PBS SA together with source/path/site predictors. In this case the site predictor consists of a geology-based site class (A, B, C or D), but another predictor variable such as $V_{S,30}$ could be used. Here, T^* is the crossover period separating the LF PBS band from the HF band. We then add correlated within-event residuals sampled from a covariance model to reproduce the target cross-period and cross-component dependence.

(2) Simulation of non-stationary stochastic HF signals. HF waveforms are generated using an approach similar to Sabetta et al. (2021). The duration of the stochastic signals and the parameters of their time envelope are computed from each simulated low-frequency signal.

(3) Merging and adjustment. The stochastic HF signals are merged with the PBS signals in the frequency domain using complementary low-pass/high-pass filters with a transition band centered at f_{merge}, chosen slightly below the maximum resolvable simulation frequency f_{max}. A frequency-domain adjustment (spectral matching with PGA correction) is then applied to match the target SA from step (1). Because spectral matching and PGA correction may introduce displacement drift, the adjusted BB signals are re-merged with the original PBS signals to preserve the LF content and any permanent displacement captured by the PBS. This adjustment-remerge loop is repeated until the mismatch between the target and BB SA falls below a prescribed threshold.

For this case study, an Iceland-specific ANN was trained using the transfer learning technique, with $T^*=$ 1 s. For the two June 2000 South Iceland earthquakes, the correlated within-event residual field was simulated conditional on the recorded $SA(T < T^*)$; therefore, at recording stations there is an exact match of $SA(T < T^*)$. For the scenario earthquakes, the residual field is simulated unconditionally. For the merging in step (3), we use $f_{merge} = 1.5$ Hz given that $f_{max} = 1.9$ Hz. Further details on the ANN2BB method are provided in Hernández-Aguirre et al. (2026).

VALIDATION WITH THE 2000 SOUTH ICELAND EARTHQUAKES

Comparison with records in time and frequency domain

Figure 6 (June 21 M_w 6.4 earthquake) and Figure S4 (June 17 M_w 6.5 earthquake) compare recorded and simulated BB velocities at selected stations (see locations in Figure 2) in both the time and frequency domains, the latter represented by the FAS. To preserve permanent displacement, the recordings were processed using the baseline-correction method of Rupakhety et al. (2010); Figure S5 shows displacements from the June 21 event at some near-fault stations. We observe that the simulations generally agree well with the recordings in terms of amplitudes, arrival times, and duration at most stations. Notably, the near-fault impulsive signals are well reproduced. In the spectral domain, agreement between simulated and recorded FAS is also generally good.

Goodness-of-Fit Scores

Because for these simulations the ANN2BB conditioning enforces an exact match of the target $SA(T < T^*)$ at the recording stations, we assess performance using only the LF PBS results (low-pass filtered at f_{max}), thereby avoiding a biased evaluation of the BB stage and isolating the effects of the rupture generator and wave-propagation model. The overall performance of the LF PBS was quantitatively estimated for each station through Goodness-of-Fit (GoF) criteria (Anderson, 2004), considering the significant duration, $D_{5\text{–}75}$ (interval between 5–75% of Arias intensity), and a selection of LF horizontal IMs, namely Peak Ground Velocity (PGV), Peak Ground Displacement (PGD), SA at periods $T = 1.0$, 1.5, and 2.5 s, and the mean GoF score. The GoF scores for the simulation of the 21 June 2000 event are presented in Figure 7 for the rotation-invariant (RotInv) IMs (Rupakhety and Sigbjörnsson, 2013), which closely approximate the RotD50 IM. Overall, the GoF scores indicate good-to-excellent performance (scores > 6). Among the criteria, significant duration and PGV achieve the highest scores, whereas $SA(1\text{ s})$ consistently yields the lowest, though it still falls within the fair-to-excellent range for most stations. Similar results are obtained for the 17 June 2000 earthquake, shown in Figure S6.

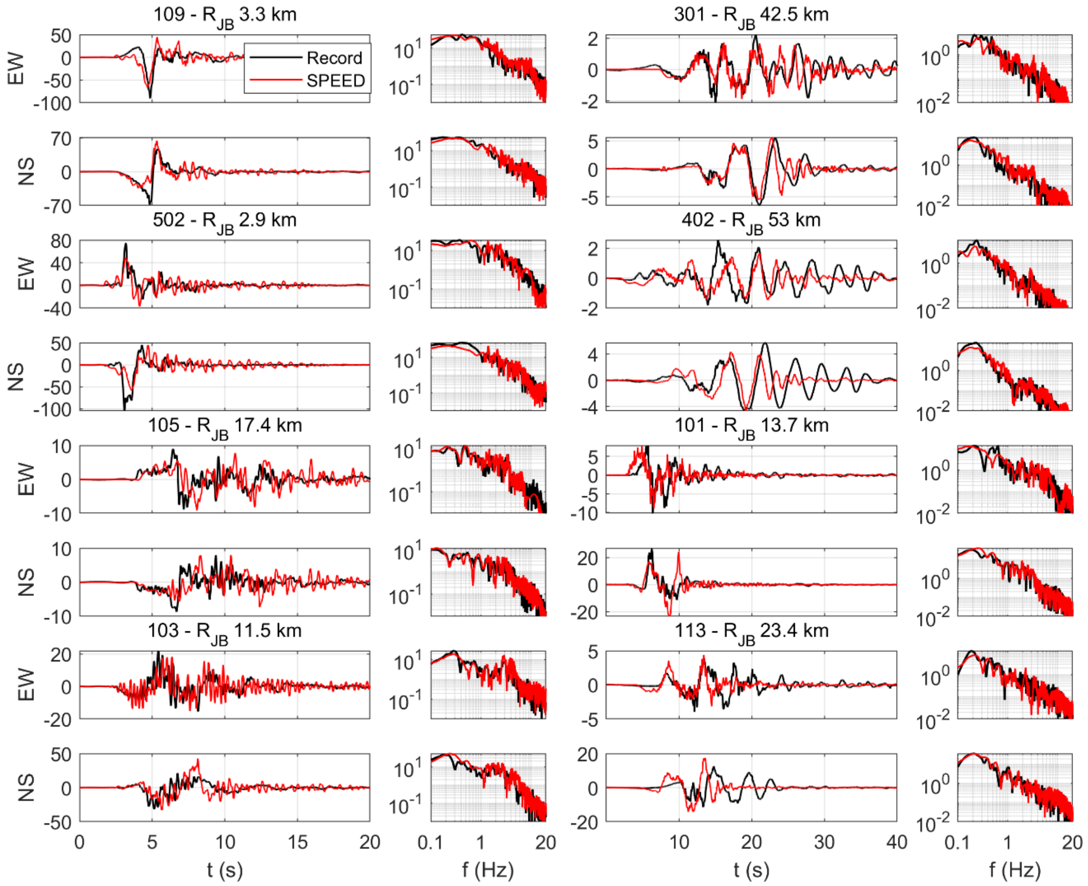

Figure 6. Comparison between recorded and simulated broadband velocity waveforms (in cm/s) and their corresponding Fourier amplitude spectra FAS (in cm), at some selected stations (see Figure 2) from the 21 June 2000 M_w 6.4 earthquake.

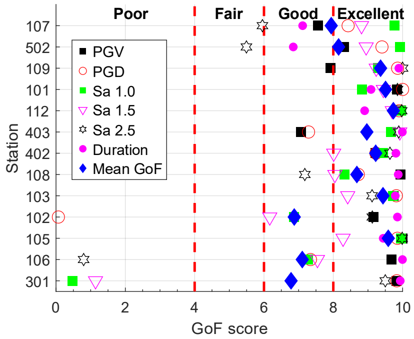

Figure 7. GoF scores for the 21 June 2000 earthquake computed for the RotInv IMs Duration ($D_{5\text{-}75}$), PGV, PGD, SA at T = 1.0, 1.5, and 2.5 s, and the mean GoF. GoF scores of 0-4 indicate a poor match, 4-6 fair, 6-8 good, and 8-10 excellent.

Ground shaking maps

For a better insight of the numerical results, Figure 8 shows computed shaking maps for the 21 June earthquake in terms of BB RotD50 PGA, SA(1 s) and SA(2 s), while Figure S7 shows maps for the vertical component. Recorded values are shown as well, using the same palette. The maps provide a clear picture of the radiation patterns associated with the focal mechanism and its interaction with the subsurface geology and topography. Although the ruptures are bilateral, since the hypocenter is close to the center of the fault, a subtle directivity is observed, leading to slightly higher amplitudes towards the north, where a greater portion of the slip is concentrated. Moreover, a strong polarization of the long-period spectral accelerations is obtained at long periods; the FN component is stronger towards the north and the south of the fault, while the FP component is stronger in the direction perpendicular to the fault (not shown for brevity). Since vertical GM is mostly associated with P waves, maps in Figure S7 show a clear four-lobed pattern resembling the P-wave radiation pattern, that at short periods becomes less evident. Vertical GM is comparable to the horizontal one in the near-source field, consistent with observational evidences (Gülerce and Abrahamson, 2011).

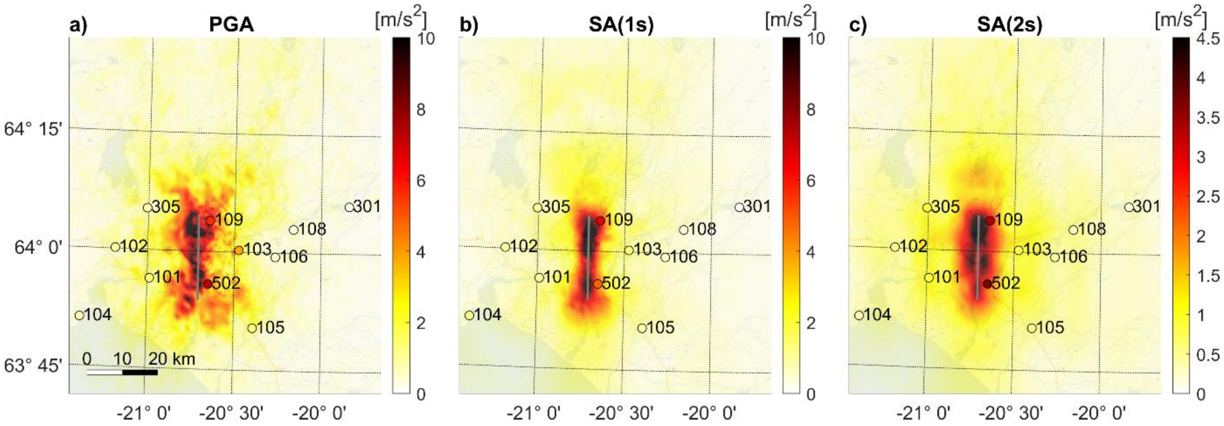

Figure 8. Computed ground-shaking maps of RotD50 PGA (a), SA(1 s) (b), SA(2 s) for the 21 June 2000 earthquake. Recorded peak values are shown with circles colored with the same palette. The fault trace is shown with a grey line.

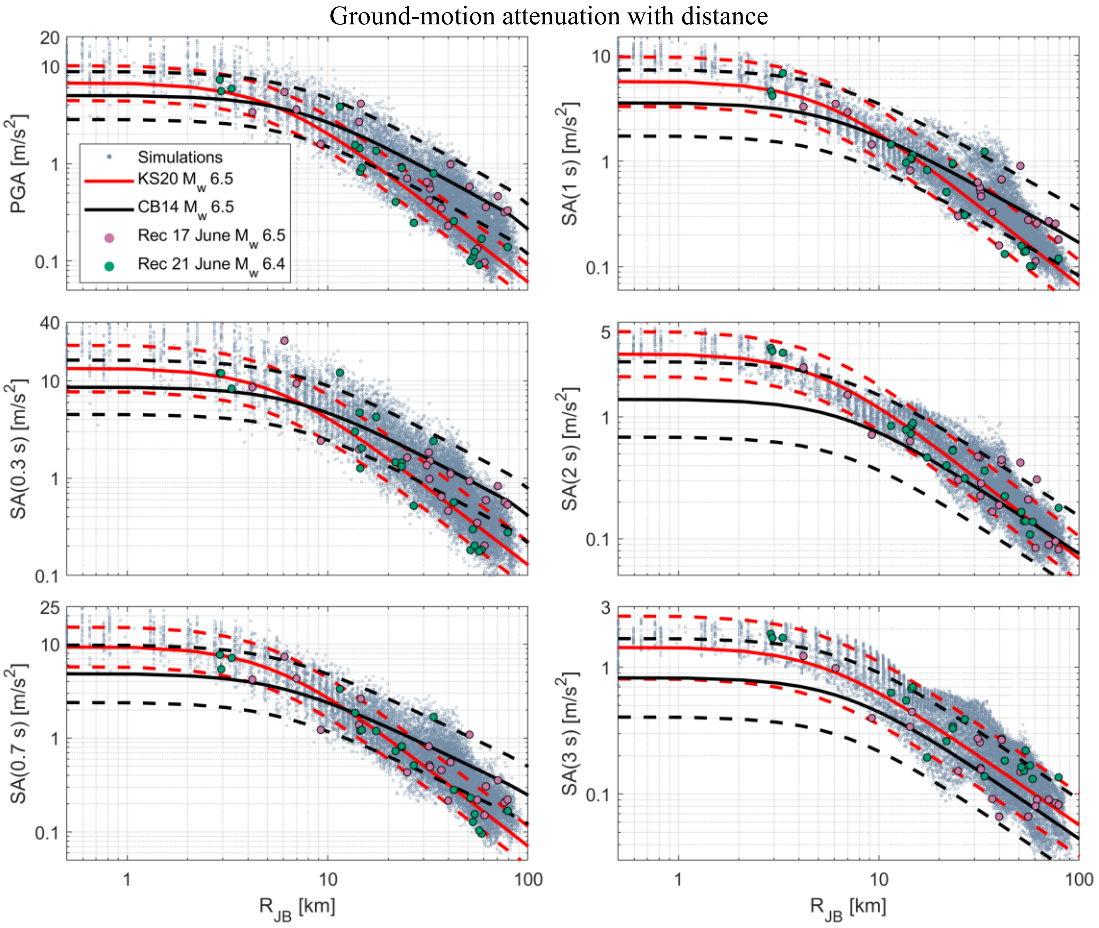

Figure 9 shows horizontal RotD50 SA for different short periods as a function of Joyner-Boore distance R_{JB}, from recordings and BB simulations. We also show the estimates from the GMM by Campbell & Bozorgnia (CB14; 2014) using VS,30=700 m/s, and from the local GMM 'F' by Kowsari et al. (KS20; 2020) for "rock". SA from KS20 corresponds to RotInv. It should be noted that the short-periods on left are mostly influenced by the stochastic part of the GM coming from the application of the ANN2BB method, while the long-periods on the right are mostly influenced by the PBS. The following comments can be made from these comparisons:

- The good agreement between simulated and recorded spectral values provides evidence that the simulation framework produces realistic period-dependent amplitude scaling and distance trends, albeit with the caveat that the short-period content is inferred (from the ANN) rather than deterministically simulated;
- Since the GMM KS20 was calibrated using the IceSMN dataset, of which almost half of the records are from the June 2000 South Iceland earthquakes, this model fits the recordings well;
- For short periods, the GMM CB14 underestimates GM at short distances and overestimates it further away from the source, which is a common trend for GMMs calibrated from data outside Iceland (e.g., Ólafsson and Sigbjörnsson, 2006);
- For long periods (2 s and 3 s), recordings and simulations in the near-field are close to the 84th percentile estimate by CB14. This is due to a source effect: large stress drop and asperities create coherent long-period seismic waves, which produce large long-period SA;
- Finally, while in the near-field the topography is relatively flat, areas with large SA(1 s) between 20 to 40 km coincide with high-elevation zones, thus caused by topographic amplification, for instance at Búrfell, Hekla, and the mountains in the northern part of the model (see Figure 2).

Figure S8 presents a comparison of vertical SA across several periods as a function of R_{JB}. No GMM is shown because a vertical-SA GMM is not currently available for Iceland. In general, there is a very good agreement between simulated and recorded spectral values for all periods and distances, except for SA(3 s) at distances larger than 20 km, which are slightly underpredicted. We observe that vertical PGA can be considerable, hence, efforts should be devoted to building a local GMM for vertical GM.

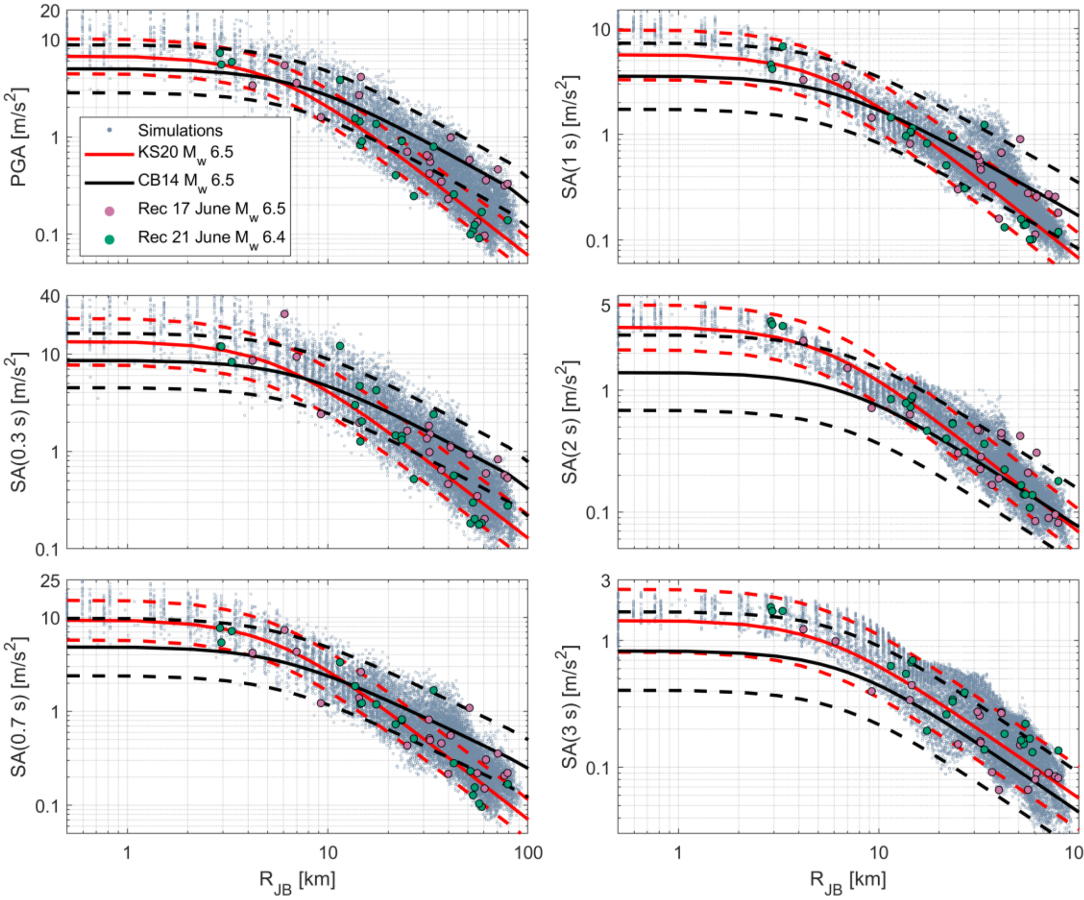

Figure 9. Attenuation of BB RotD50 SA (PGA, 0.3 s, 0.7 s, 1 s, 2s and 3 s) of the 2000 South Iceland earthquakes from recordings (dots), simulations (points), and from the GMMs by Campbell & Bozorgnia (CB14; 2014) (black lines) and Kowsari et al. (KS20, 2020) (red lines), including median ±1 σ shown with dashed lines.

GROUND-MOTION SCENARIOS

Response spectral IMs and peak parameters have been the subject of important validation exercises over the past decade (Dreger et al., 2015; Lee et al., 2020; Stupazzini et al., 2021). A robust and adaptable validation approach is to compute residuals for IMs relative to regionally applicable GMMs. Following the notation of Al Atik et al. (2010), the general expression of a GMM for an earthquake e and station s can be written as

$$\ln \mathrm{IM}_{\mathrm{es}} = \mathrm{f}_{\mathrm{es}} + \Delta \qquad (8)$$

where $\ln \mathrm{IM}_{\mathrm{es}}$ denotes the natural logarithm of the IM for event e and station s (recorded when available and simulated for the scenario ensembles); f_{es} is the median GMM prediction in log space as a function of event/source, path, and site predictors, and Δ is the total residual. The residual term can be further decomposed into fixed and random components as

$$\ln \mathrm{IM}_{\mathrm{es}} = \mathrm{f}_{\mathrm{es}} + \mathrm{a} + \delta \mathrm{B}_{\mathrm{e}} + \delta \mathrm{W}_{\mathrm{es}} \qquad (9)$$

where, a is the model bias, δB_e is the between-event residual with zero mean and variance τ^2, and δW_{es} is the within-event residual with zero mean and variance ϕ^2. δB_e captures the systematic deviation between observations and the bias-corrected median prediction for a given event, while the within-event residual δW_{es} reflects the deviation between observations and the bias- and event-corrected median prediction for a specific record from event e at site s. Consequently, the total residual has mean a and variance $\sigma^2 = \tau^2 + \phi^2$. δW_{es} can be further broken down into a systematic site-to-site residual and a remaining within-event residual which represents factors which are not accounted for.

In the following we compare RotD50 spectral ordinates from scenario simulations with KS20 and CB14, and we summarize total residuals and their partition into between-event and within-event components. For a consist comparison with KS20, we do not further decompose the within-event term.

Comparison with GMMs

For a consistent comparison between the simulated scenario earthquakes and the GMMs KS20 and CB14, we fit the simulated RotD50 spectral accelerations using a simple mixed-effects GMM estimated by maximum likelihood. In this formulation, Eq. (10) defines the fixed-effects median prediction f_{es} (for each oscillator period T):

$$\ln \mathrm{SA}(\mathrm{T}) = c_1 + c_2 \cdot \mathrm{M_w} + c_3 \cdot \ln\sqrt{{\mathrm{R_{JB}}}^2 + \mathrm{h}^2} + c_{SC}\mathrm{SC}, \tag{10}$$

where h=6 km and SC is a binary indicator for the geology-based site classes used in the broadband extension at short periods. The mixed-effects model includes an event-specific random intercept $\delta B_e \sim \mathcal{N}(0, \tau^2)$ and a record-level residual $\delta W_{es} \sim \mathcal{N}(0, \phi^2)$. The resulting fixed-effects coefficients for selected oscillator periods are reported in Table S1.

Figure S9 compares the M_w 6.5 scenario simulations with recordings from the 2000 South Iceland earthquakes, the fitted GMM (for SC=B), and the reference GMMs KS20 and CB14. Across most periods and distances, the fitted attenuation trends are close to KS20, with modest underprediction at short periods and short distances; overall, the simulated levels remain broadly consistent with the Icelandic recordings, while the tendency of CB14 noted previously is also apparent. Figure S10 presents the corresponding comparison for the M_w 7 scenarios. Because no M_w 7 strong-motion recordings are available from Iceland, we include strike-slip recordings with M_w 7–7.1 from the NESS dataset (Darfield 2010 and Ridgecrest 2019; Sgobba et al., 2021) as an external reference, rather than a direct regional validation dataset. The M_w 7 simulations and their fitted trends lie systematically below KS20 across periods and distances, and the increase in short-period SA relative to the M_w 6.5 ensemble is limited, suggesting magnitude saturation in the simulated motions; this behavior is not captured by KS20, which uses a linear magnitude scaling, and cannot be robustly constrained with the currently available Icelandic dataset. Despite the lower median level relative to KS20, the simulated spectral ordinates are generally within the range of the NESS records for most periods, although at longer periods the simulations tend to occupy the upper part of the observed range and the fitted trends exceed CB14. At very short distances ($R_{JB} < 3$ km) and T=2–3 s, the fitted M_w 7 medians are approximately a factor of ~2.5 above CB14. A plausible explanation is that the adopted M_w 7 fault dimensions are smaller than average for that magnitude, which implies higher stress drop (Eshelby, 1957) and stronger long-period source radiation due to the concentration of slip over a smaller area.

To summarize these comparisons across periods, Figure 10 reports the total residuals of the simulations relative to KS20 and CB14, shown as mean bias ± one standard deviation (panels a–b), together with distance-dependent residual trends relative to KS20 for PGA and SA(2 s) (panels c–d), distinguishing the M_w 6.5 and M_w 7 ensembles.

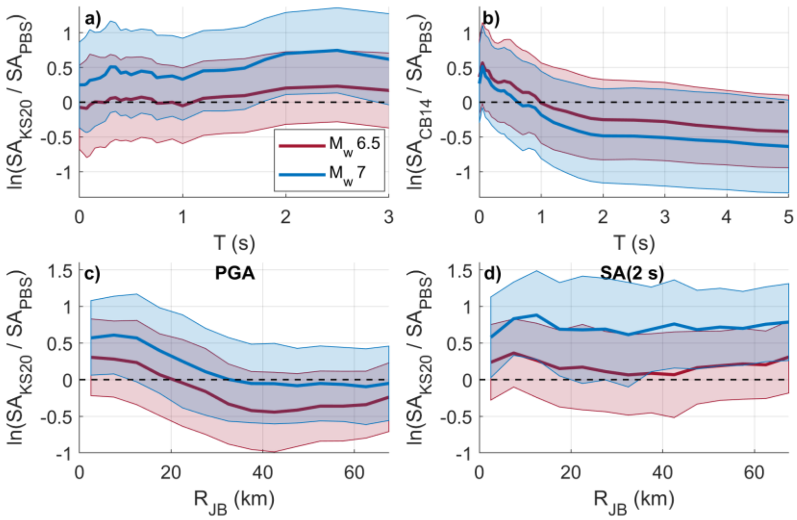

Figure 10. Total residuals relative to KS20 (a) and CB14 (b) as a function of period, shown with variability bands corresponding to the median ± one standard deviation. Panels (c) and (d) show residuals relative to KS20 as a function of R_{JB} for PGA and SA(2 s), respectively.

Variance components

We estimate variance components from the mixed-effects model fitted to the simulations; we do not estimate variance components by residualizing against KS20 because its site representation with only two site classes would leave additional site effects in the residuals and artificially inflate ϕ. Figure 11 summarizes the resulting variability components (τ, ϕ, σ) as a function of period and compares them with the corresponding components reported by KS20 and CB14. This decomposition therefore quantifies the variability produced by the simulation ensemble and provides a consistency check against empirical models. The comparison indicates that the magnitude of the simulated variability is broadly consistent with empirical expectations across periods: the total σ and its partition into τ and ϕ fall within the range spanned by the GMMs, supporting the use of the scenario ensembles for hazard and risk applications where variability is important, since it controls the rate of extreme ground-motion realizations.

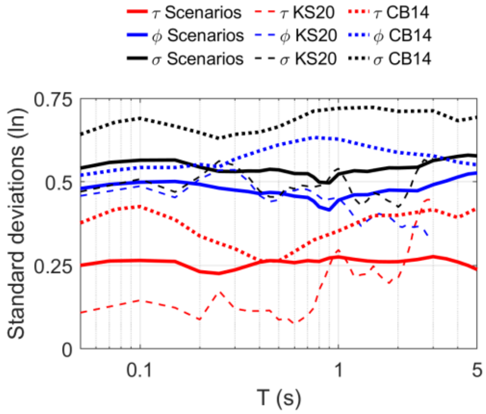

Figure 11. Components of standard deviation of scenario simulations by this study (solid lines), KS20 (thin dashed lines), and CB14 (dotted lines).

Although not shown here for brevity, the simulations indicate that between-scenario variability is controlled not only by rupture intensity, represented here by $\overline{\Delta\sigma}$, but also by the spatial distribution of slip. Scenarios with larger $\overline{\Delta\sigma}$ and shallow asperities (e.g., scenario 30) generate systematically higher GM amplitudes than scenarios with lower $\overline{\Delta\sigma}$ and smaller or deeper slip concentrations (e.g., scenario 15). In particular, shallow high-slip patches enhance radiation from the most energetic portions of the rupture and can strengthen directivity-related effects at favorable azimuths. This highlights the value of the rupture generator for producing ensembles of physically plausible ground-motion scenarios that capture variability associated with source heterogeneity beyond that represented in GMMs through scalar source metrics alone.

DISCUSSION

Rupture generator

A central contribution of this study is a kinematic rupture generator that represents rupture complexity through correlated stochastic spatial fields. Slip, rupture speed (expressed as $\mathrm{V_R/V_S}$), and peak slip velocity ($\mathrm{V_{max}}$) are modeled as spatially heterogeneous parameters with prescribed marginal distributions and two-point structure, while enforcing cross-field dependence using the joint covariance model of Savran and Olsen (2020). This allows the GM simulations to incorporate uncertainty in source parameters and the effects of small-scale rupture heterogeneity, which are important contributors to high-frequency excitation. The adopted covariance model assumes isotropic correlation and was calibrated from dynamic-rupture simulations of strike-slip earthquakes in the M_w 6.5–7.2 range; consequently, its transferability to substantially different magnitudes and other faulting styles remains uncertain and should be evaluated in future work.

In the generator, the slip distribution is prescribed first (deterministic, stochastic or hybrid) and the remaining fields are generated conditionally so that the simulated $\mathrm{V_R/V_S}$ and $\mathrm{V_{max}}$ remain statistically consistent with the imposed slip distribution. This conditional simulation, mathematically equivalent to conditioning a joint Gaussian prior on a fixed realization, preserves the cross-field correlations encoded in the covariance matrix even when the prescribed slip field does not strictly follow the prior autocorrelation model. While this choice relaxes the requirement that slip obey the same two-point statistics as the prior, it provides a practical way to simulate historical events with prescribed slip distributions while retaining physically motivated inter-parameter coupling. This is particularly relevant for near-fault applications, where directivity and coherency are highly sensitive to the coupled variability of $\mathrm{V_R}$, $\mathrm{V_{max}}$, and slip.

Epistemic uncertainty in $\mathrm{V_{max}}$ remains influential because it exerts first-order control on simulated GM amplitudes and frequency content. Consequently, limited constraints on its marginal distribution and its scaling with magnitude, faulting style, and tectonic stress conditions remain an important source of uncertainty. In the present framework, we partially represent this uncertainty by sampling an effective stress drop parameter from a magnitude-conditioned lognormal distribution and using it as a physically motivated proxy for rupture intensity (assumed proportional to $\mathrm{V_{max}}$). This approach spans plausible amplitude levels and propagates uncertainty in rupture strength into the simulations. Reducing this uncertainty will require improved constraints on $\mathrm{V_{max}}$ from empirical studies and/or dynamic-rupture simulations.

Moreover, the results presented here are obtained using a two-stage GM simulation framework: (1) low-frequency deterministic PBS and (2) broadband extension via ANN2BB method. Therefore, results should be interpreted as evaluating the end-to-end workflow. Within this workflow, the rupture generator controls rupture patterns, directivity, and long-period radiation in the PBS component, and it also influences the ANN2BB-predicted short-period SA through the long-period PBS inputs used to generate broadband time histories.

Scenario ensembles

The M_w 6.5 scenario ensemble produces median attenuation trends close to the local KS20 GMM (Figure 10). In contrast, M_w 7 simulations are generally lower than KS20. Because KS20 was calibrated using data with $M_w \leq 6.5$, its extrapolation to M_w 7 is only weakly constrained; in this magnitude range, the simulations provide a physically motivated alternative where empirical data are sparse. We note that short-period motions are strongly influenced by the ANN2BB extension, and discrepancies at short periods reflect both the ANN mapping and the LF PBS inputs that encode rupture directivity and long-period energy. The ANN was trained in two stages: first on a global dataset and then fine-tuned using the same local dataset employed to calibrate KS20. Therefore, discrepancies at short periods may reflect (i) genuine magnitude-scaling differences not captured by KS20, (ii) the scaling of rupture parameters that control the long-period PBS ground motions used as inputs to ANN2BB, and/or (iii) limitations in how the ANN generalizes magnitude scaling beyond the effective range represented by the local data. By contrast, long-period GM is governed by the deterministic PBS. Overall, these results underscore the value of simulation-based ensembles for providing a physics-informed characterization of shaking in the M_w–distance range where empirical constraints are limited, thereby helping to bound epistemic uncertainty associated with extrapolating GMMs beyond their M_w calibration range and with using ergodic GMMs (such as CB14) in regions with specific tectonic and geologic features such as Iceland.

Ground-motion variability

Beyond median trends, the scenarios allow evaluation of the variability of SA with distance and period. The fact that the standard deviations are comparable to local and global GMMs (Figure 11) is a key outcome for hazard and risk applications, because accurately capturing variability governs the occurrence rate of extreme ground-motion realizations and ensures that simulations represent the full distribution of outcomes rather than only median trends. The larger τ obtained relative to KS20 is likely attributable to the limited number of events used to calibrate KS20, which can bias between-event variability estimates downward when the event sample is small. Overall, the agreement in σ and its decomposition suggests that the range of rupture realizations considered in this study reproduces a realistic variability of ground motions.

CONCLUSIONS

This article presents a modular framework for physics-based ground-motion simulation that couples (i) a kinematic rupture generator with correlated heterogeneous fields for slip, V_R/V_S, and V_{max}, (ii) low-frequency (LF) 3D PBS, and (iii) a broadband extension via ANN2BB. The rupture generator enables efficient sampling of physically plausible rupture variability while preserving inter-parameter dependence through prescribed one- and two-point statistics, providing a practical mechanism to propagate epistemic uncertainty in rupture parameters into simulated ground motions. The framework is intentionally modular: its marginal statistics, scaling relations, and correlation structure can be updated as improved constraints become available.

The LF simulations were validated using the June 2000 M_w 6.5 and M_w 6.4 South Iceland earthquakes. SPEED was used to model wave propagation in a heterogeneous 3-D crustal volume (138 km × 90 km × 25 km) up to ~1.9 Hz (≈46 million spectral nodes). Goodness-of-fit results support the adequacy of the regional model and source representation in the frequency band directly simulated.

Broadband scenario ensembles derived from LF PBS + ANN2BB reproduce local-GMM trends at M_w 6.5, but indicate systematically lower long-period shaking for M_w 7 than obtained by extrapolating the local GMM beyond its calibration range. Given the absence of $M_w > 6.5$ observations in the regional dataset, this discrepancy is consequential: it suggests potential bias in empirical extrapolation and points to source-physics effects that empirical fits derived from smaller events may not capture. Moreover, widely used ergodic GMMs such as CB14 show a clear bias when compared to recorded and simulated spectral accelerations in Iceland. Overall, the simulations provide physically grounded constraints on magnitude scaling and variability that can supplement sparse recordings and help bound epistemic uncertainty in scenario-based and probabilistic seismic hazard and risk analyses. In practice, the proposed workflow can be used to generate region-specific, non-ergodic ground-motion ensembles for engineering applications, including scenario-based risk studies and the development of PBS-informed inputs to PSHA where empirical constraints are limited.

Data and Resources

The rupture generator and a manual are available at https://github.com/vicmoyhdz/PDRG. The mesh was created using a python tool available at http://github.com/vicmoyhdz/CubitPython4SPEED. The SPEED code used for the simulations is available at http://speed.mox.polimi.it. The electronic supplement to this article provides a description of the procedure to simulate stochastic fields V_{max} and V_R/V_S conditioned on a given slip field. Moreover, we include supporting figures introduced in the article. The simulation results are available from the corresponding author on reasonable request.

Acknowledgements

Computer resources were provided by UTS at the University of Iceland through the Icelandic Research e-Infrastructure project (IREI). This work was financed by the SERICE project funded by a Grant of Excellence from the Icelandic Centre for Research (RANNIS), Grant Number: 218149-051.

References

Abercrombie, R. E., 2021, Resolution and uncertainties in estimates of earthquake stress drop and energy release, Phil Trans R Soc A, 379, doi: 10.1098/rsta.2020.0131.

Aki, K., 1972, Earthquake mechanism, Tectonophysics, 13, no. 1, 423–446, doi: https://doi.org/10.1016/0040-1951(72)90032-7.

Akinci, A., A. Pitarka, P. Artale Harris, P. De Gori, and M. Buttinelli, 2024, Impact of the Earthquake Rupture on Ground-Motion Variability of the 24 August 2016 Mw 6.2 Amatrice, Italy, Earthquake, Bull. Seismol. Soc. Am., 114, no. 6, 2823–2845, doi: 10.1785/0120240002.

Al Atik, L., N. Abrahamson, J. J. Bommer, F. Scherbaum, F. Cotton, and N. Kuehn, 2010, The variability of ground-motion prediction models and its components, Seismol. Res. Lett., 81, no. 5, 794–801, doi: 10.1785/gssrl.81.5.794.

Anderson, J. G., 2004, Quantitative measure of the Goodness-Of-Fit of synthetic seismograms, Proc. 13th World Conf. Earthq. Eng.

Aquib, T. A., J. C. Vyas, and P. M. Mai, 2025, Pseudo-Dynamic Source Characterization for Geometrically Rough Faults Using Machine Learning, Bull. Seismol. Soc. Am.

Baltay, A., S. Ide, G. Prieto, and G. Beroza, 2011, Variability in earthquake stress drop and apparent stress: energetic and enervated earthquakes, Geophys. Res. Lett., 38, no. 6, doi: 10.1029/2011GL046698.

Bayat, F., M. Kowsari, and B. Halldorsson, 2022, A new 3-D finite-fault model of the Southwest Iceland bookshelf transform zone, Geophys. J. Int., 231, no. 3, 1618–1633, doi: 10.1093/gji/ggac272.

Beresnev, I. A., 2022, Spatial Heterogeneity of Fault Slip and the Radiated Spectra of Ground Motions, Bull. Seismol. Soc. Am., 112, no. 3, 1463–1471, doi: 10.1785/0120210235.

Bizzarri, A., 2012, Rupture speed and slip velocity: What can we learn from simulated earthquakes?, Earth Planet. Sci. Lett., 317–318, 196–203, doi: 10.1016/j.epsl.2011.11.023.

Bjarnason, I. Th., and P. Einarsson, 1991, Source mechanism of the 1987 Vatnafjöll Earthquake in south Iceland, J. Geophys. Res. Solid Earth, 96, no. B3, 4313–4324, doi: 10.1029/90JB00831.

Boore, D. M., 1983, Stochastic Simulation of High-Frequency Ground Motions Based on Seismological Models of the Radiated Spectra, Bull. Seismol. Soc. Am., 73, no. 6, 1865–1894.

Brune, J. N., 1970, Tectonic Stress and the Spectra of Seismic Shear Waves from Earthquakes, J. Geophys. Res., 75, no. 26, 4997–5009.

Campbell, K. W., and Y. Bozorgnia, 2014, NGA-West2 Ground Motion Model for the Average Horizontal Components of PGA, PGV, and 5% Damped Linear Acceleration Response Spectra, Earthq. Spectra, 30, no. 3, 1087–1114, doi: 10.1193/062913EQS175M.

Candela, T., F. Renard, Y. Klinger, K. Mair, J. Schmittbuhl, and E. E. Brodsky, 2012, Roughness of Fault Surfaces over Nine Decades of Length Scales, J. Geophys. Res. Solid Earth, 117, no. B8, 2011JB009041, doi: 10.1029/2011JB009041.

Causse, M., L. A. Dalguer, and P. M. Mai, 2014, Variability of dynamic source parameters inferred from kinematic models of past earthquakes, Geophys. J. Int., 196, no. 3, 1754–1769, doi: 10.1093/gji/ggt478.

Clifton, A., and P. Einarsson, 2005, Styles of surface rupture accompanying the June 17 and 21, 2000 earthquakes in the South Iceland Seismic Zone, Tectonophysics, 396, nos. 3–4, 141–159, doi: 10.1016/j.tecto.2004.11.007.

Coreform-LLC, 2025, Cubit (Version 2024.3) [Computer Software]. https://coreform.com.

Cotton, F., R. Archuleta, and M. Causse, 2013, What is Sigma of the Stress Drop?, Seismol. Res. Lett., 84, no. 1, 42–48, doi: 10.1785/0220120087.

Crempien, J. G. F., and R. J. Archuleta, 2017, Within-Event and Between-Events Ground Motion Variability from Earthquake Rupture Scenarios, Pure Appl. Geophys., 174, no. 9, 3451–3465, doi: 10.1007/s00024-017-1615-x.

Darzi, A., B. Halldorsson, F. Cotton, and S. Rahpeyma, 2024, Nationwide frequency-dependent seismic site amplification models for Iceland, Soil Dyn. Earthq. Eng., 183, doi: 10.1016/j.soildyn.2024.108798.

Decriem, J., T. Árnadóttir, A. Hooper, H. Geirsson, F. Sigmundsson, M. Keiding, B. G. Ófeigsson, S. Hreinsdóttir, P. Einarsson, P. LaFemina, *et al.*, 2010, The 2008 May 29 earthquake doublet in SW Iceland, Geophys. J. Int., 181, no. 2, 1128–1146, doi: 10.1111/j.1365-246X.2010.04565.x.

Detweiler, S. T., and A. M. Wein, 2018, The HayWired Earthquake Scenario—Engineering Implications (Ver. 1.1, April 2022), U.S. Geological Survey Scientific Investigations Report 2017–5013–I–Q.

Dreger, D. S., G. C. Beroza, S. M. Day, C. A. Goulet, T. H. Jordan, P. A. Spudich, and J. P. Stewart, 2015, Validation of the SCEC Broadband Platform V14.3 Simulation Methods Using Pseudospectral Acceleration Data, Seismol. Res. Lett., 86, no. 1, 39–47, doi: 10.1785/0220140118.

Dubois, L., K. L. Feigl, D. Komatitsch, T. Árnadóttir, and F. Sigmundsson, 2008, Three-dimensional mechanical models for the June 2000 earthquake sequence in the south Iceland seismic zone, Tectonophysics, 457, nos. 1–2, 12–29, doi: 10.1016/j.tecto.2008.05.020.

Dunham, E. M., D. Belanger, L. Cong, and J. E. Kozdon, 2011, Earthquake Ruptures with Strongly Rate-Weakening Friction and Off-Fault Plasticity, Part 2: Nonplanar Faults, Bull. Seismol. Soc. Am., 101, no. 5, 2308–2322, doi: 10.1785/0120100076.

Eshelby, J. D., 1957, The Determination of the Elastic Field of an Ellipsoidal Inclusion, and Related Problems, Proc Roy Soc A241, 241, 376–396.

Geller, R. J., 1976, Scaling relations for earthquake source parameters and magnitudes, Bull. Seismol. Soc. Am., 66, no. 5, 1501–1523.

Graves, R., T. H. Jordan, S. Callaghan, E. Deelman, E. Field, G. Juve, C. Kesselman, P. Maechling, G. Mehta, K. Milner, *et al.*, 2011, CyberShake: A Physics-Based Seismic Hazard Model for Southern California, Pure Appl. Geophys., 168, nos. 3–4, 367–381, doi: 10.1007/s00024-010-0161-6.

Graves, R., and A. Pitarka, 2010, Broadband ground-motion simulation using a hybrid approach, Bull. Seismol. Soc. Am., 100, no. 5 A, 2095–2123, doi: 10.1785/0120100057.

Graves, R., and A. Pitarka, 2016, Kinematic Ground-Motion Simulations on Rough Faults Including Effects of 3D Stochastic Velocity Perturbations, Bull. Seismol. Soc. Am., 106, no. 5, 2136–2153, doi: 10.1785/0120160088.

Graves, R., and A. Pitarka, 2015, Refinements to the Graves and Pitarka (2010) Broadband Ground-Motion Simulation Method, Seismol. Res. Lett., 86, no. 1, 75–80, doi: 10.1785/0220140101.

Guatteri, M., P. M. Mai, and G. C. Beroza, 2004, A Pseudo-Dynamic Approximation to Dynamic Rupture Models for Strong Ground Motion Prediction, Bull. Seismol. Soc. Am., 94, no. 6, 2051–2063.

Guatteri, M., P. M. Mai, G. C. Beroza, and J. Boatwright, 2003, Strong Ground-Motion Prediction from Stochastic-Dynamic Source Models, Bull. Seismol. Soc. Am., 93, no. 1, 301–313.

Gülerce, Z., and N. A. Abrahamson, 2011, Site-Specific Design Spectra for Vertical Ground Motion, Earthq. Spectra, 27, no. 4, 1023–1047, doi: 10.1193/1.3651317.

Harris, R. A., 2004, Numerical Simulations of Large Earthquakes: Dynamic Rupture Propagation on Heterogeneous Faults, Pure Appl. Geophys., 161, nos. 11–12, 2171–2181, doi: 10.1007/s00024-004-2556-8.

Hensch, M., B. Lund, T. Árnadóttir, and B. Brandsdóttir, 2016, Temporal stress changes associated with the 2008 May 29 M_W 6 earthquake doublet in the western South Iceland Seismic Zone, Geophys. J. Int., 204, no. 1, 544–554, doi: 10.1093/gji/ggv465.

Hernández-Aguirre, V. M., R. Rupakhety, R. Paolucci, M. Vanini, and C. Smerzini, 2026, Hybrid broadband ground-motion simulation using neural networks with spatial, inter-period, and cross-component correlations, EarthArXiv, doi: 10.31223/X5H76R.

Ida, Y., 1972, Cohesive force across the tip of a longitudinal-shear crack and Griffith's specific surface energy, J. Geophys. Res. 1896-1977, 77, no. 20, 3796–3805, doi: 10.1029/JB077i020p03796.

Imperatori, W., and P. M. Mai, 2012, Sensitivity of broad-band ground-motion simulations to earthquake source and Earth structure variations: an application to the Messina Straits (Italy): Sensitivity of broad-band ground-motion, Geophys. J. Int., 188, no. 3, 1103–1116, doi: 10.1111/j.1365-246X.2011.05296.x.

Jónasson, K., B. Bessason, Á. Helgadóttir, P. Einarsson, G. B. Guðmundsson, B. Brandsdóttir, K. S. Vogfjörd, and K. Jónsdóttir, 2021, A harmonised instrumental earthquake catalogue for Iceland and the northern Mid-Atlantic Ridge, Nat. Hazards Earth Syst. Sci., 21, no. 7, 2197–2214, doi: 10.5194/nhess-21-2197-2021.

Kowsari, M., S. Ghasemi, F. Bayat, and B. Halldorsson, 2023, A backbone seismic ground motion model for strike-slip earthquakes in Southwest Iceland and its implications for near- and far-field PSHA, Bull. Earthq. Eng., 21, no. 2, 715–738, doi: 10.1007/s10518-022-01556-z.

Kowsari, M., T. Sonnemann, B. Halldorsson, B. Hrafnkelsson, J. Snæbjörnsson, and S. Jónsson, 2020, Bayesian inference of empirical ground motion models to pseudo-spectral accelerations of south Iceland seismic zone earthquakes based on informative priors, Soil Dyn. Earthq. Eng., 132, doi: 10.1016/j.soildyn.2020.106075.

Lee, R. L., B. A. Bradley, P. J. Stafford, R. Graves, and A. Rodriguez-Marek, 2020, Hybrid Broadband Ground Motion Simulation Validation of Small Magnitude Earthquakes in Canterbury, New Zealand, Earthq. Spectra, 36, no. 2, 673–699, doi: 10.1177/8755293019891718.

Liu, P., and R. J. Archuleta, 2004, A new nonlinear finite fault inversion with three-dimensional Green's functions: Application to the 1989 Loma Prieta, California, earthquake, J. Geophys. Res. Solid Earth, 109, no. B2, 2003JB002625, doi: 10.1029/2003JB002625.

Liu, P., R. J. Archuleta, and S. H. Hartzell, 2006, Prediction of broadband ground-motion time histories: Hybrid low/high-frequency method with correlated random source parameters, Bull. Seismol. Soc. Am., 96, no. 6, 2118–2130, doi: 10.1785/0120060036.

Madariaga, R., 1977, High-Frequency Radiation from Crack (Stress Drop) Models of Earthquake Faulting, Geophys. J. Int., 51, no. 3, 625–651, doi: 10.1111/j.1365-246X.1977.tb04211.x.

Mai, P. M., 2000, Source Scaling Properties from Finite-Fault-Rupture Models, Bull. Seismol. Soc. Am., 90, no. 3, 604–615, doi: 10.1785/0119990126.

Mai, P. M., and G. C. Beroza, 2002, A spatial random field model to characterize complexity in earthquake slip, J. Geophys. Res. Solid Earth, 107, no. B11, doi: 10.1029/2001jb000588.

Mai, P. M., M. Galis, K. K. S. Thingbaijam, J. C. Vyas, and E. M. Dunham, 2017, Accounting for Fault Roughness in Pseudo-Dynamic Ground-Motion Simulations, Pure Appl. Geophys., 174, no. 9, 3419–3450, doi: 10.1007/s00024-017-1536-8.

Manighetti, I., M. Campillo, C. Sammis, P. M. Mai, and G. King, 2005, Evidence for Self-similar, Triangular Slip Distributions on Earthquakes: Implications for Earthquake and Fault Mechanics, J. Geophys. Res. Solid Earth, 110, no. B5, 2004JB003174, doi: 10.1029/2004JB003174.

Mavroeidis, G. P., and A. S. Papageorgiou, 2010, Effect of Fault Rupture Characteristics on Near-Fault Strong Ground Motions, Bull. Seismol. Soc. Am., 100, no. 1, 37–58, doi: 10.1785/0120090018.

Mazzieri, I., M. Stupazzini, R. Guidotti, and C. Smerzini, 2013, SPEED: SPectral Elements in Elastodynamics with Discontinuous Galerkin: A Non-Conforming Approach for 3d Multi-Scale Problems, Int. J. Numer. Methods Eng., 95, no. 12, 991–1010, doi: 10.1002/nme.4532.

Melgar, D., and G. P. Hayes, 2019, The Correlation Lengths and Hypocentral Positions of Great Earthquakes, Bull. Seismol. Soc. Am., 109, no. 6, 2582–2593, doi: 10.1785/0120190164.

Menke, W., V. Levin, and R. Sethi, 1995, Seismic attenuation in the crust at the mid-Atlantic plate boundary in south-west Iceland, Geophys. J. Int., 122, no. 1, 175–182, doi: 10.1111/j.1365-246X.1995.tb03545.x.

Moschetti, M. P., E. M. Thompson, and K. Withers, 2024, Basin Effects from 3D Simulated Ground Motions in the Greater Los Angeles Region for Use in Seismic Hazard Analyses, Earthq. Spectra, 40, no. 2, 1042–1065, doi: 10.1177/87552930241232372.

Oglesby, D. D., and S. M. Day, 2002, Stochastic Fault Stress: Implications for Fault Dynamics and Ground Motion, Bull. Seismol. Soc. Am., 92, no. 8, 3006–3021.

Ogorodnikov, V. A., and S. M. Prigarin, 1996, Numerical Modelling of Random Processes and Fields: Algorithms and Applications, De Gruyter, Berlin, Boston.

Ohnaka, M., and T. Yamashita, 1989, A cohesive zone model for dynamic shear faulting based on experimentally inferred constitutive relation and strong motion source parameters, J. Geophys. Res. Solid Earth, 94, no. B4, 4089–4104, doi: https://doi.org/10.1029/JB094iB04p04089.

Olafsdottir, E. A., S. Erlingsson, and B. Bessason, 2023, Hybrid non-invasive characterization of soil strata at sites with and without embedded lava rock layers in the South Iceland Seismic Zone, Bull. Eng. Geol. Environ., 82, no. 4, doi: 10.1007/s10064-023-03136-0.

Paolucci, R., F. Gatti, M. Infantino, C. Smerzini, A. G. Özcebe, and M. Stupazzini, 2018, Broadband ground motions from 3D physics-based numerical simulations using artificial neural networks, Bull Seism. Soc Am, 108, no. 3, 1272–1286, doi: 10.1785/0120170293.

Paolucci, R., C. Smerzini, M. Vanini, I. Mazzieri, V. M. Hernández-Aguirre, and L. Vadacca, 2026, Near-source ground motion from normal faults: insights from the physics-based numerical simulations of the 1980 Irpinia earthquake, Southern Italy, Earthq. Spectra.

Pitarka, A., R. Graves, K. Irikura, K. Miyakoshi, C. Wu, H. Kawase, A. Rodgers, and D. McCallen, 2022, Refinements to the Graves–Pitarka Kinematic Rupture Generator, Including a Dynamically Consistent Slip-Rate Function, Applied to the 2019 Mw 7.1 Ridgecrest Earthquake, Bull. Seismol. Soc. Am., 112, no. 1, 287–306, doi: 10.1785/0120210138.

Power, W. L., and T. E. Tullis, 1991, Euclidean and Fractal Models for the Description of Rock Surface Roughness, J. Geophys. Res. Solid Earth, 96, no. B1, 415–424, doi: 10.1029/90JB02107.

Rupakhety, R., B. Halldorsson, and R. Sigbjörnsson, 2010, Estimating coseismic deformations from near source strong motion records: Methods and case studies, Bull. Earthq. Eng., 8, no. 4, 787–811, doi: 10.1007/s10518-009-9167-9.

Rupakhety, R., and S. Ólafsson, 2015, IceSMN Icelandic Strong Motion Network [Data set], Int. Fed. Digit. Seismogr. Netw., doi: 10.7914/YW8C-NY36.

Rupakhety, R., and R. Sigbjörnsson, 2013, Rotation-invariant measures of earthquake response spectra, Bull. Earthq. Eng., 11, no. 6, 1885–1893, doi: 10.1007/s10518-013-9472-1.

Rupakhety, R., R. Sigbjörnsson, and S. Ólafsson, 2016, Damage to residential buildings in Hveragerði during the 2008 Ölfus Earthquake: simulated and surveyed results, Bull. Earthq. Eng., 14, no. 7, 1945–1955, doi: 10.1007/s10518-015-9783-5.

Sabetta, F., A. Pugliese, G. Fiorentino, G. Lanzano, and L. Luzi, 2021, Simulation of Non-Stationary Stochastic Ground Motions Based on Recent Italian Earthquakes, Bull. Earthq. Eng., 19, no. 9, 3287–3315, doi: 10.1007/s10518-021-01077-1.

Savran, W. H., and K. B. Olsen, 2020, Kinematic Rupture Generator Based on 3-D Spontaneous Rupture Simulations Along Geometrically Rough Faults, J. Geophys. Res. Solid Earth, 125, no. 10, e2020JB019464, doi: 10.1029/2020JB019464.

Schmedes, J., R. J. Archuleta, and D. LavalÍee, 2013, A kinematic rupture model generator incorporating spatial interdependency of earthquake source parameters, Geophys. J. Int., 192, no. 3, 1116–1131, doi: 10.1093/gji/ggs021.

Schmedes, J., R. J. Archuleta, and D. Lavallée, 2010, Correlation of earthquake source parameters inferred from dynamic rupture simulations, J. Geophys. Res. Solid Earth, 115, no. 3, doi: 10.1029/2009JB006689.

Sgobba, S., C. Felicetta, G. Lanzano, F. Ramadan, M. D'Amico, and F. Pacor, 2021, NESS2.0: An Updated Version of the Worldwide Dataset for Calibrating and Adjusting Ground-Motion Models in Near Source, Bull. Seismol. Soc. Am., 111, no. 5, 2358–2378, doi: 10.1785/0120210080.

Shi, Z., and S. M. Day, 2013, Rupture dynamics and ground motion from 3-D rough-fault simulations, J. Geophys. Res. Solid Earth, 118, no. 3, 1122–1141, doi: 10.1002/jgrb.50094.

Sigbjörnsson, R., and R. Rupakhety, 2014, A saga of the 1896 South Iceland earthquake sequence: Magnitudes, macroseismic effects and damage, Bull. Earthq. Eng., 12, no. 1, 171–184, doi: 10.1007/s10518-013-9579-4.

Somerville, P. G., N. F. Smith, R. W. Graves, W.-C. F. Services, and N. A. Abrahamson, 1997, Modification of Empirical Strong Ground Motion Attenuation Relations to Include the Amplitude and Duration Effects of Rupture Directivity, Seismol. Res. Lett., 68, no. 1, 199–222.

Song, S. G., 2016, Developing a generalized pseudo-dynamic source model of M_w 6.5–7.0 to simulate strong ground motions, Geophys. J. Int., 204, no. 2, 1254–1265, doi: 10.1093/gji/ggv521.

Song, S. G., L. A. Dalguer, and P. M. Mai, 2014, Pseudo-dynamic source modelling with 1-point and 2-point statistics of earthquake source parameters, Geophys. J. Int., 196, no. 3, 1770–1786, doi: 10.1093/gji/ggt479.

Spudich, P., and B. S. J. Chiou, 2008, Directivity in NGA Earthquake Ground Motions: Analysis Using Isochrone Theory, Earthq. Spectra, 24, no. 1, 279–298, doi: 10.1193/1.2928225.

Spudich, P., and L. N. Frazer, 1984, Use of Ray Theory to Calculate High-Frequency Radiation from Earthquake Sources Having Spatially Variable Rupture Velocity and Stress Drop, Bull. Seismol. Soc. Am., 74, no. 6, 2061–2082.

Stupazzini, M., M. Infantino, A. Allmann, and R. Paolucci, 2021, Physics-based probabilistic seismic hazard and loss assessment in large urban areas: A simplified application to Istanbul, Earthq. Eng. Struct. Dyn., 50, no. 1, 99–115, doi: 10.1002/eqe.3365.

Sung, C.-H., N. Morikawa, A. Iwaki, N. Abrahamson, and H. Miyake, 2025, Ground-Motion Models Incorporating Nonergodic Effects from 3D Numerical Simulations in Japan, Bull. Seismol. Soc. Am., 115, no. 4, 1852–1875, doi: 10.1785/0120240239.

Thingbaijam, K. K. S., and P. M. Mai, 2016, Evidence for Truncated Exponential Probability Distribution of Earthquake Slip, Bull. Seismol. Soc. Am., 106, no. 4, 1802–1816, doi: 10.1785/0120150291.

Thingbaijam, K. K. S., P. Martin Mai, and K. Goda, 2017, New Empirical Earthquake Source-Scaling Laws, Bull. Seismol. Soc. Am., 107, no. 5, 2225–2246, doi: 10.1785/0120170017.

Tinti, E., 2005, A Kinematic Source-Time Function Compatible with Earthquake Dynamics, Bull. Seismol. Soc. Am., 95, no. 4, 1211–1223, doi: 10.1785/0120040177.

Supplementary Material: “A kinematic rupture generator for ground-motion simulations: Validation and scenarios in South Iceland”

Victor M. Hernández-Aguirre[1] · Rajesh Rupakhety[1] Roberto Paolucci[3] · Chiara Smerzini[3] · Manuela Vanini[3] · Bjarni Bessason[2] · Sigurður Erlingsson[2]

*Corresponding author email: victorh@hi.is

[1] Earthquake Engineering Research Center, University of Iceland, Selfoss, Iceland

[2] Faculty of Civil and Environmental Engineering, University of Iceland, Reykjavík, Iceland

[3] Department of Civil and Environmental Engineering, Politecnico di Milano, Milan, Italy

In this electronic supplement we provide a description of the procedure to simulate stochastic fields V_{max} and V_R/V_S conditioned on a given slip field. Moreover, we include supporting figures introduced in the article. These figures include details on the mesh (Figure S1), examples of rupture models for M_w 7 scenarios (Figure S3), the rupture model (Figure S2) and results for the 17 June 2000 M_w 6.5 earthquake (Figure S4 and6), results related to the vertical component (Figure S7 and Figure S8) and results from the scenario simulations (Table S1, Figure S9 and Figure S10).

Procedure to Simulate Stochastic Fields V_{max} and V_R/V_S

Naming V_{max}, and V_R/V_S as the random variables Z_2 and Z_3, respectively, the steps to simulate realizations z_2 and z_3 conditioned on a given slip distribution (X) are the following:

1. Convert the non-Gaussian slip distribution X into a Gaussian random field Z_1, by applying a normal score transformation. First, map the marginal distribution of X into the uniform interval [0,1], such that its cumulative distribution function (CDF) is $U=F_X(X)$, where $U\sim\mathcal{U}(0,1)$. The uniform variable is then mapped into Gaussian space using the inverse of the standard normal CDF, $Z_1=\Phi^{-1}(U)$, such that $Z_1\sim\mathcal{N}(0,1)$. This transformation preserves the rank order of the original values while ensuring Gaussian marginals.
2. Construct a covariance matrix Σ of the standard multivariate Gaussian PDF for Z_1, Z_2 and Z_3, for instance from the model of Savran and Olsen (2020) or Song (2016)

$$\Sigma = \begin{bmatrix} \Sigma_{11} & \Sigma_{12} & \Sigma_{13} \\ \Sigma_{21} & \Sigma_{22} & \Sigma_{23} \\ \Sigma_{31} & \Sigma_{32} & \Sigma_{33} \end{bmatrix}$$

3. Partition the joint Gaussian

$$\Sigma_{23,1} = \begin{bmatrix} \Sigma_{21} \\ \Sigma_{31} \end{bmatrix}, \qquad \Sigma_{23,23} = \begin{bmatrix} \Sigma_{22} & \Sigma_{23} \\ \Sigma_{32} & \Sigma_{33} \end{bmatrix}, \quad \Sigma_{1,23} = \Sigma_{23,1}^{T} = [\Sigma_{12} \quad \Sigma_{13}].$$

4. Form the conditional distribution of $Z_{23|1}(Z_1 = z_1)\sim\mathcal{N}(\mu_{23|1}, \Sigma_{23|1})$, with

$$\mu_{23|1} = \Sigma_{23,1}\,\Sigma_{11}^{-1}\,(Z_1),$$

$$\Sigma_{23|1} = \Sigma_{23,23} - \Sigma_{23,1}\,\Sigma_{11}^{-1}\,\Sigma_{1,23},$$

   where $\mu_{23|1}$ and $\Sigma_{23|1}$ are the conditional mean and covariance.

5. Perform Cholesky factorization of the conditional covariance matrix

$$\Sigma_{23|1} = LL^{T}.$$

6. Draw a random sample $z_{23|1}^{(s)}$ from $Z_{23|1}$ as

$$z_{23|1}^{(s)} = \mu_{23|1} + L\,\varepsilon,$$

where $\varepsilon\sim\mathcal{N}(0, I)$, of size 2·M·N, where M·N is the number of subfaults. Vector $z_{23|1}^{(s)}$ is then reshaped back to the 2 fields z_2 and z_3 of size M·N.

7. The outputs from the previous step are two standard Gaussian fields, which are then transformed to the target marginal distributions, as described in the article.

Additional Figures

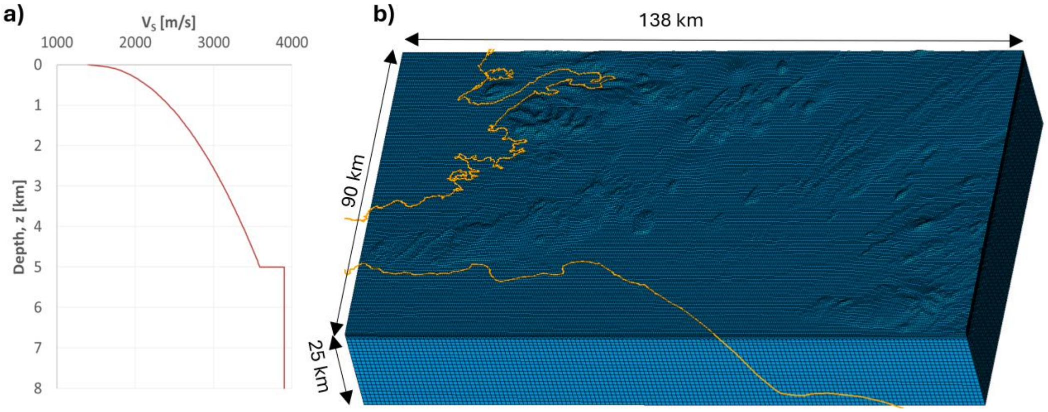

Figure S1.a) Adopted shear-wave velocity model. b) Three-dimensional mesh for South Iceland consisting of 1.67×10^6 hexahedral elements. The orange line represents the coastline.

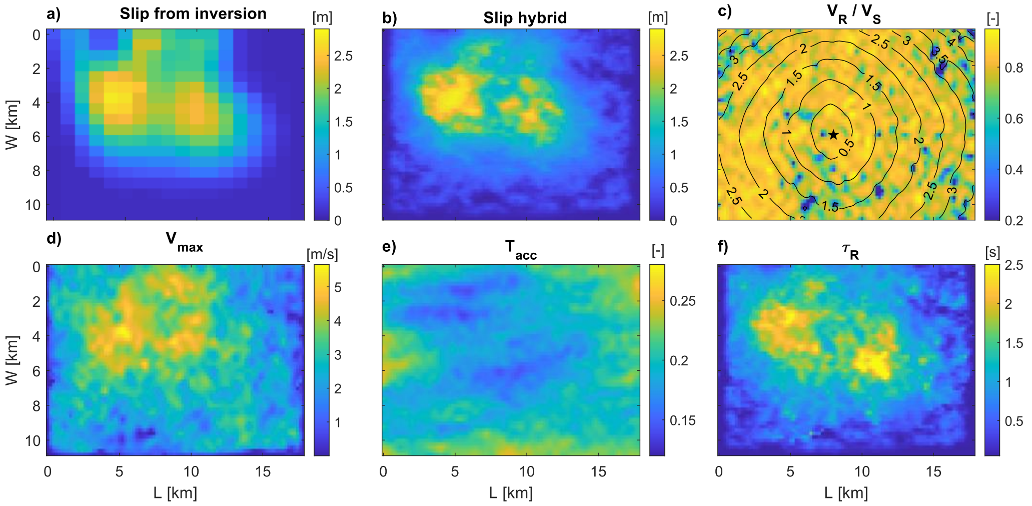

Figure S2. Kinematic source parameters for the 17 June 2000 M_w 6.5 earthquake. (a) Deterministic slip obtained from Dubois et al. (2008). (b) Hybrid slip distribution. The distributions of V_R/V_S (c) and V_{max} (d) are generated from a joint distribution conditioned on the slip. T_{acc} (e) is a prescribed as a correlated random field with V_{max}. τ_R (f) is the rise time The contour lines in panel (c) represent T_R, while the star is the hypocenter location.

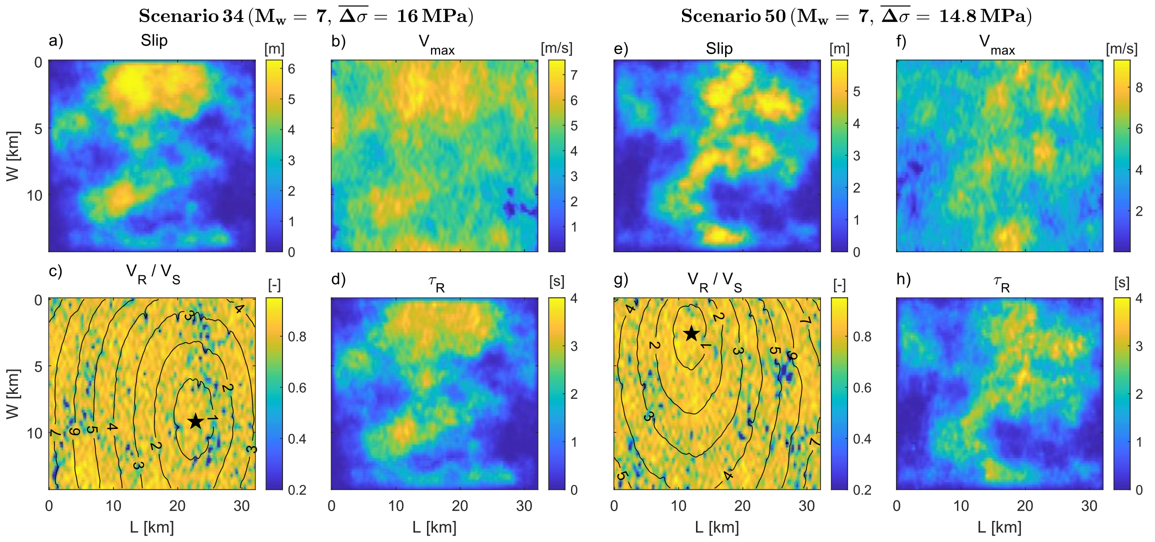

Figure S3. Kinematic source parameters for M_w 7 earthquake scenarios 34 (panels a to d) and 50 (panels e to h).

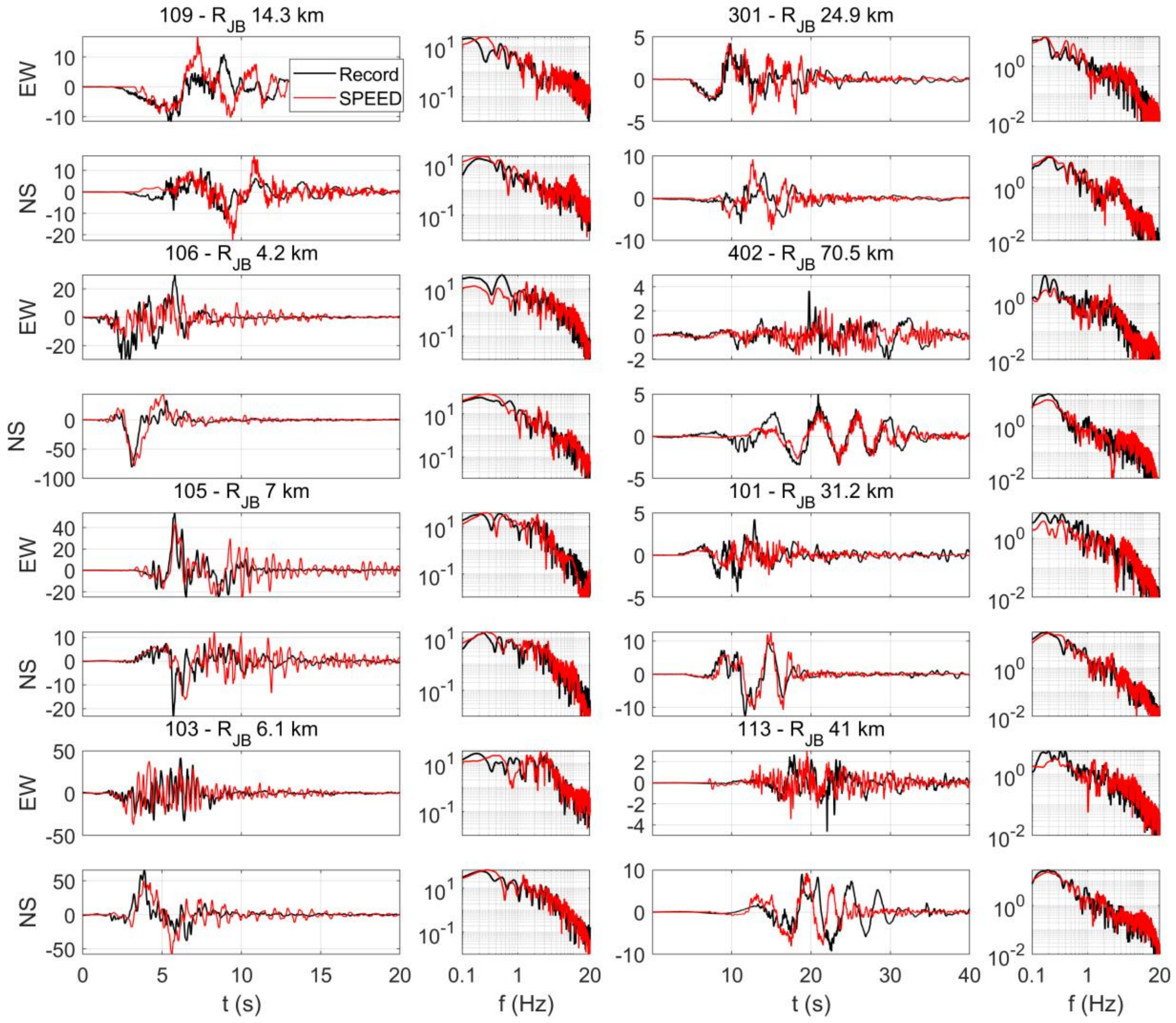

Figure S4. Comparison between broadband recorded and simulated velocity waveforms (in cm/s) and their corresponding FAS (in cm), at some selected stations from the 17 June 2000 M_w 6.5 earthquake.

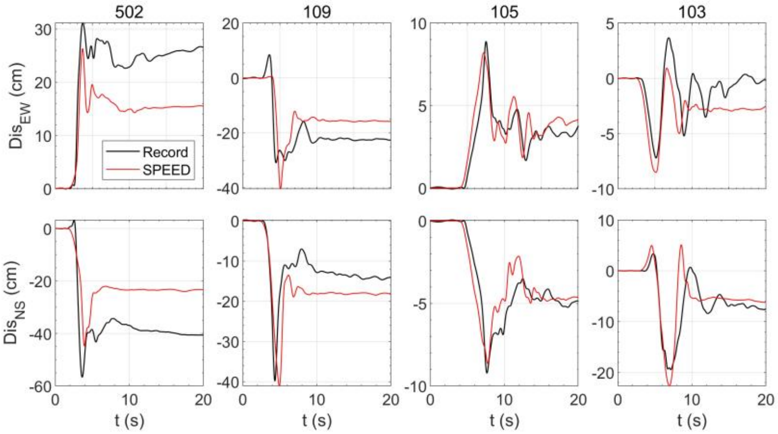

Figure S5. Comparison between recorded and simulated displacements from the 21 June 2000 earthquake at some near-fault stations.

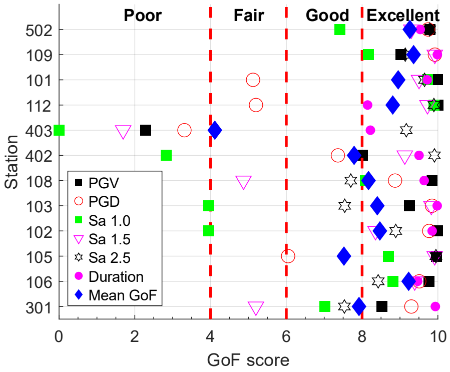

Figure S6. GoF scores for the 17 June 2000 earthquake computed for the RotInv measures of Duration ($D_{5\text{-}75}$), PGV, PGD, SA at T = 1.0, 1.5, and 2.5 s, and the mean GoF for various recording stations. GoF scores of 0-4 indicate a poor match, 4-6 fair, 6-8 good, and 8-10 excellent.

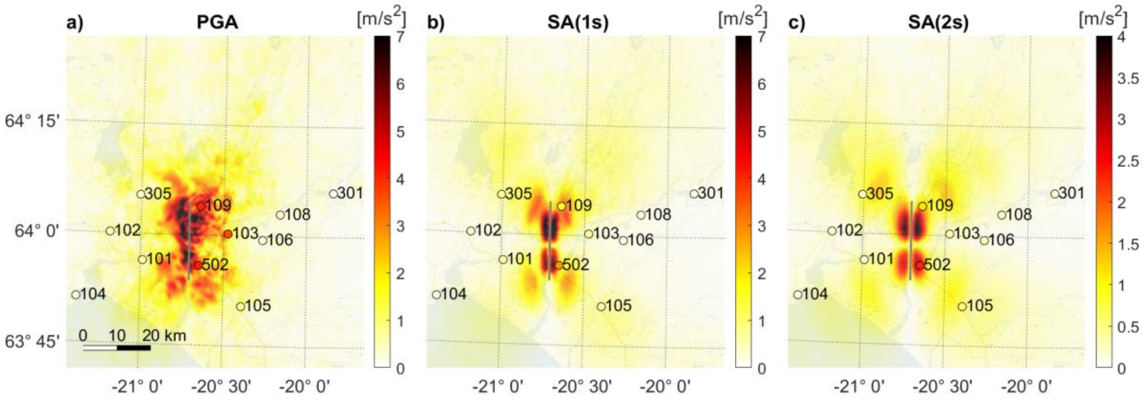

Figure S7. Computed ground-shaking maps of vertical PGA (a), SA(1 s) (b), SA(2 s) for the 21 June 2000 earthquake. Recorded peak values are shown with circles coloured with the same palette. The fault trace is shown with a grey line.

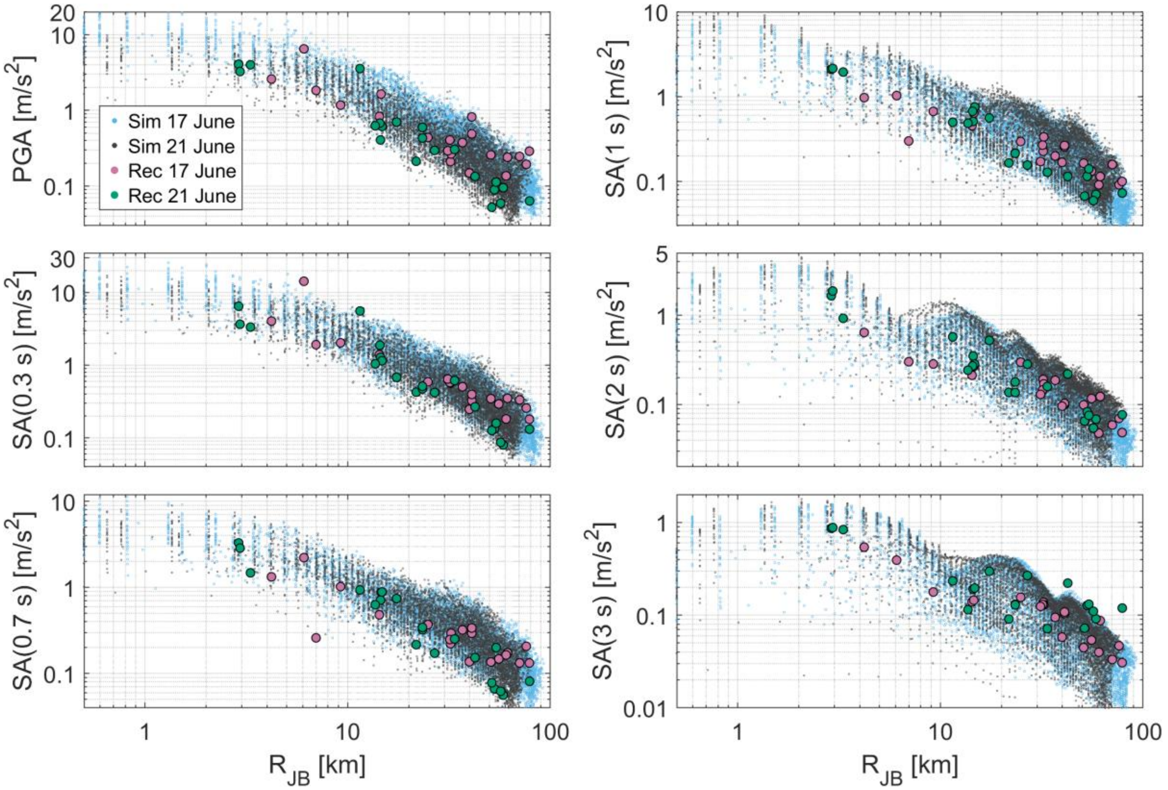

Figure S8. Attenuation of vertical SA (PGA, 0.3 s, 0.7 s, 1 s, 2s and 3 s) from recordings and simulations of the 2000 South Iceland earthquakes.

Table S1. Coefficients of the GMM (Eq. 10) fitted to the earthquake scenarios.

T	c_1	c_2	c_3	c_B	c_C	c_D
PGA	0.699	0.447	-1.274	0.253	0.480	0.175
0.3	1.373	0.423	-1.248	0.239	0.488	0.160
0.7	-0.201	0.667	-1.404	0.196	0.398	0.109
1	-0.611	0.688	-1.354	0.095	0.054	-0.010
2	-3.517	1.048	-1.336	-	-	-
3	-5.146	1.196	-1.282	-	-	-

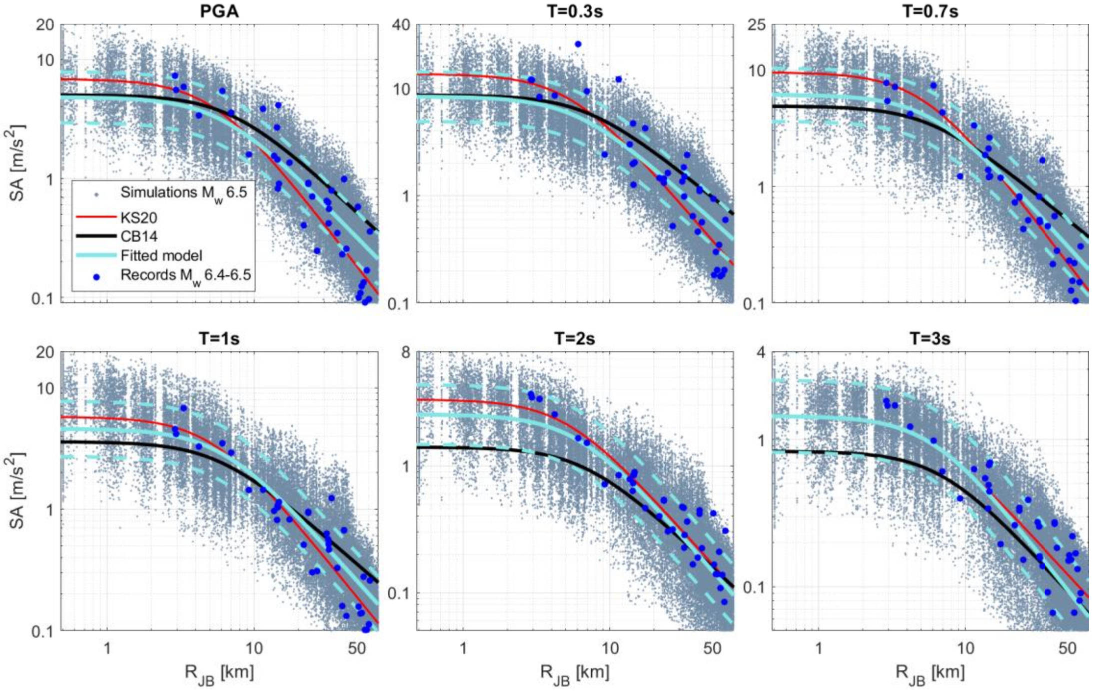

Figure S9. Comparison of SA attenuation with distance from M_w 6.5 scenarios for multiple oscillator periods, showing estimates from GMMs KS20 (Kowsari et al., 2020) and CB14 (Campbell & Bozorgnia, 2014) versus a simple regression model (eq. 10) fitted to the simulations. Records from the 2000 South Iceland earthquakes are represented by the blue dots.

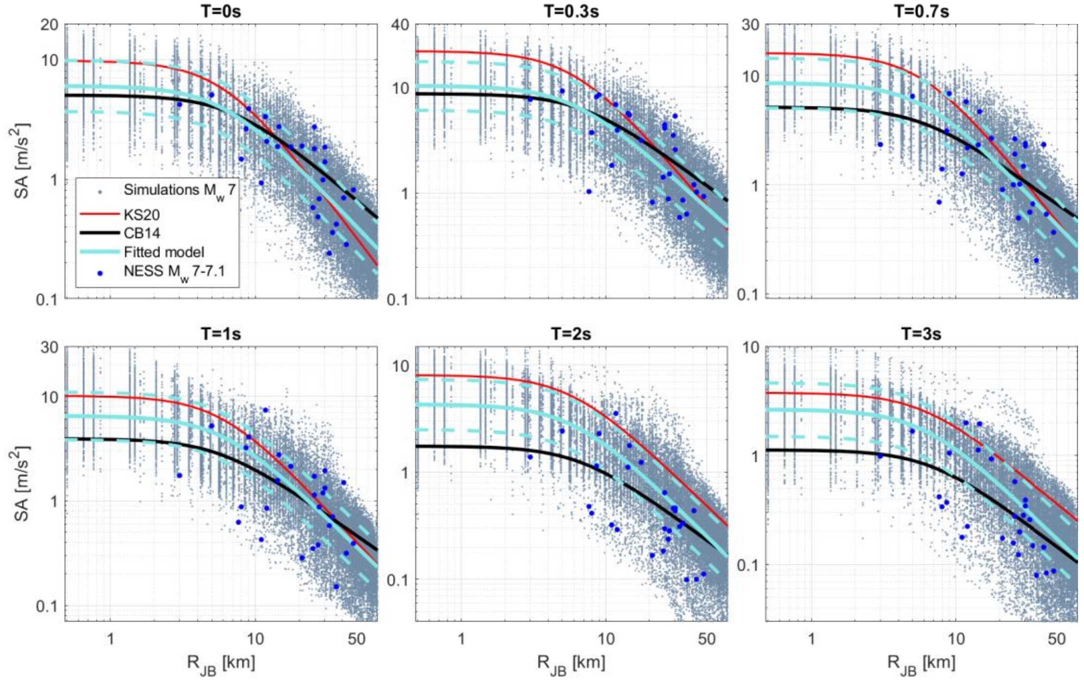

Figure S10. Comparison of SA attenuation with distance from M_w 7 scenarios for multiple oscillator periods, showing estimates from GMMs KS20 and CB14 versus a simple regression model (eq. 10) fitted to the simulations. For reference, the blue dots are SAs from strike-slip earthquakes with M_w 7-7.1 from the NESS dataset (Sgobba et al., 2021).